Biodegradation of Ancient Organic Carbon Fuels Seabed Methane Emission at the Arctic Continental Shelves

A manuscript prepared for *Journal of Geophysical Research: Solid Earth*

Kehua You

Institute for Geophysics, Jackson School of Geosciences, the University of Texas at Austin, Austin, TX 78712, United States

Email: khyouml@gmail.com

Key points:

1. A numerical model is developed to simulate the coupled thermal, hydrological, microbial and chemical processes in the subsea permafrost.
2. Biodegradation of the ancient organic carbon in the thawing permafrost results in seabed microbial methane emission.
3. Seabed methane emission is less likely caused by methane hydrate dissociation at the Arctic continental shelves.

Abstract: This study explores the carbon stability in the Arctic permafrost following the sea level transgression since the Last Glacial Maximum (LGM). Arctic permafrost is a significant natural reservoir of greenhouse gas which is stored in frozen organic carbon, methane hydrates and natural gas reservoirs. Post-LGM sea level transgression resulted in ocean water, which is up to 20 ^{o}C warmer compared to the average annual air mass, inundating, and thawing the permafrost. This study develops a one-dimensional multiphase flow, multicomponent transport numerical model and apply it to investigate the coupled thermal, hydrological, microbial, and chemical processes occurring in the thawing permafrost. Results show that microbial methane is produced and vented to the seawater immediately upon the flooding of the Arctic continental shelves. This microbial methane is generated by biodegradation of the previously frozen organic carbon in the thawing permafrost. The maximum seabed methane flux is predicted in the shallow water where the sediment has been warmed up, but the remaining amount of organic carbon is still high. It is less likely to induce seabed methane emission from methane hydrate dissociation. Such situation only happens when there is very shallow (~200 m depth), intra-permafrost methane hydrate, the occurrence of which is limited. This study provides insights into the limits of methane release from the ongoing flooding of the Arctic permafrost, which is critical to understand the role of the Arctic permafrost in the carbon cycle, ocean chemistry and climate change.

Keywords: Permafrost degradation, Sea level rise, Carbon cycle, Methane emission, Biodegradation of organic carbon, Methane hydrate dissociation

Plain Language Summary: Arctic permafrost stores ~1,700 billion tons of organic carbon. If just a fraction of that melts, the escaping methane would become one of the world's largest sources of greenhouse gas and would severely impact the environment and climate. Over the last ~18,000 years, a quarter of the stored organic carbon in Arctic permafrost has been flooded by the rising, warm seas. This has melted the ice and degraded the permafrost. But what happens to the carbon pools? This study investigates the stability of the carbon in Arctic permafrost following the flooding from 18,000 years before present using a newly developed numerical model. Results show that microbial methane is generated and emitted to the seawater immediately following the flooding. This methane is produced by biodegradation of the previously frozen organic carbon near the seafloor. The maximum methane emission is predicted in the shallow water near the coast where the sediment has been warmed up, but the remaining amount of organic carbon is high. This study provides insights into the limits of methane release from the ongoing flooding of the Arctic permafrost, which is critical to understand the role of the Arctic permafrost in the carbon cycle, ocean chemistry and climate change.

1. Introduction

Arctic permafrost is a significant natural reservoir of methane, a greenhouse gas 84 times more potent than carbon dioxide (CO_2) over a 20-year timeframe (Ruppel & Kessler, 2017). The total organic carbon in the Arctic permafrost is ~1700 billion tons, twice the global atmospheric pool (Miner et al., 2022; Schuur et al., 2008). When the eustatic sea level began rising sharply after the Last Glacial Maximum (LGM, ~18,000 years ago), the much warmer seawater (as much as 20 ^{o}C) flooded the Arctic permafrost and began increasing its temperature (Ruppel et al., 2010; Ruppel & Kessler, 2017). About 1/5 of the Arctic permafrost was under the warm seawater nowadays which amounts to a warming carbon stock ~1/4 of the total carbon stock in the Arctic permafrost (Sayedi et al., 2020; Schuur et al., 2015). Such warming significantly degraded the permafrost and narrowed the offshore continuous permafrost extent from far shore locations in ~120 m water depth to near shore in as shallow as ~25 m isobath (Hu et al., 2013; Nicolsky et al., 2012; Portnov et al., 2013; Ruppel et al., 2016). Permafrost degradation resulted in the widespread methane release at the shelves of the East Siberian Arctic Sea, the Laptev Sea, the Kara Sea, the Beaufort Sea, the Chuckchi Sea and the Western Svalbard margin (Cramer & Franke, 2005; Lorenson et al., 2016; Pohlman et al., 2017; Portnov et al., 2013; Shakhova et al., 2019; Shakhova, Semiletov, Salyuk, et al., 2010; Shakhova et al., 2015). Oxidation of most, if not all, of the dissolved methane within near-seafloor sediments, leads to a potentially large flux of dissolved carbon into the ocean contributing to ocean acidification (Biastoch et al., 2011; Boudreau et al., 2015; Hong et al., 2016). In addition, methane concentration can also become high enough to exceed saturation and microbial methane consumption, releasing free methane bubbles directly to the atmosphere (McGinnis et al., 2006; Ruppel & Kessler, 2017). Such methane emission may contribute to the particularly high methane concentration in the atmosphere above the Laptev Sea (2.97 ppm) and East Siberian Sea (2.66 ppm, latitudinal mean = 1.85 ppm) and amplify climate warming (Berchet et al., 2016; Lorenson et al., 2016; Shakhova et al., 2019; Shakhova, Semiletov, Salyuk, et al., 2010; Thornton et al., 2016).

The warming and thawing of the permafrost and the carbon emission is continuing now and potentially accelerates with an enhanced Arctic warming during the past ~40 years (Johannessen et al., 2004; Serreze & Francis, 2006; Smith et al., 2022). However, we still do not understand the subsea sources of methane, which determine the timing and magnitude of the

seabed methane emission and its environmental impact (Sayedi et al., 2020). The purpose of this study is to explore the stabilities of the carbon pools in the thawing subsea permafrost.

Permafrost carbon is frozen in ancient organic carbon, trapped in solid methane hydrate, and accumulated in natural gas reservoirs (Sayedi et al., 2020; Schuur et al., 2008; Serov et al., 2015). A substantial fraction of the frozen organic carbon is in yedoma deposits (Kanevskiy et al., 2011; Strauss et al., 2021; Zimov et al., 2006). Yedoma was deposited during past glacial periods (late Pleistocene) (Zimov et al., 2006). It covers more than 1 million km^2 of the north plains of Siberia and Central Alaska to an average depth 25 m (Vonk et al., 2013; Zimov et al., 2006). During the LGM when the global sea level was 120 m lower than today, similar deposits covered substantial areas of the exposed continental shelves. Yedoma deposits comprise large amounts of grass roots and animal bones, and have a carbon content from 2 wt.% to 5 wt.%, much higher than the underlying mineral soil (Zimov et al., 2006; Schadel et al., 2014). This exceptionally old organic carbon is among the most biolabile organic carbon and decomposes quickly when thawed (Vonk et al., 2013; Zimov 2006). About half of the annual methanogenesis in north Siberian lakes and most hotspot-seep methane ebullition in interior Alaska thermokarst lakes are fueled by yedoma deposits (Zimov et al., 1997; Walter Anthony et al., 2021).

Methane hydrate is an ice-like substance that is composed of methane and water molecules (Sloan & Koh, 2007). Methane hydrate is stable at high pressure and low temperature, and is widely found in marine sediments (Sloan & Koh, 2007). In Arctic permafrost, methane hydrate is stable from as shallow as 130 m and down to 2000 m (Collett et al., 2011). Methane hydrate in Arctic fills discrete layers of coarse-grained sediments beneath the permafrost with hydrate saturation between 20% and 100% (fraction of pores filled by methane hydrate) (Collett et al., 2011). Warming may dissociate methane hydrate, release free methane gas, and emit methane bubbles into the seawater (Baranov et al., 2020; Lorenson et al., 2016; Paull et al., 2011; Shakhova et al., 2019; Shakhova, Semiletov, Leifer, et al., 2010).

The Arctic stores over 1,200 Pg (10^{15} g) of thermogenic methane carbon in coal beds and natural gas deposits (Ruppel, 2015; Walter Anthony et al., 2012). The continuous permafrost forms a “cryosphere cap” which traps the gas leaking from these reservoirs. Degradation of permafrost could destroy the integrity of this “cryosphere cap” and facilitate the expulsion of methane (Walter Anthony et al., 2012).

This study develops a one-dimensional (1D) multiphase flow multicomponent numerical model to investigate the stabilities of the frozen organic carbon and methane hydrate at the Arctic continental shelves since the LGM. Applying the model to typical environmental conditions in the Arctic shows that biodegradation of the ancient organic carbon in the thawing subsea permafrost is the major source of seabed methane emission. While previous studies focused on investigating the permafrost degradation, this study takes a further step to explore the carbon stability and the methane dynamics within the permafrost system (Gavrilov et al., 2020; Malakhova & Eliseev, 2017; Nicolsky et al., 2012; Nicolsky & Shakhova, 2010; Overduin et al., 2019; Wilkenskjeld et al., 2022). The results of this study provide insights on the limits of methane release from the ongoing flooding of permafrost. Such knowledge is critical to understand the role of the Arctic permafrost in the carbon cycle, ocean chemistry and the past and future climate warming.

2. Mathematical model

A 1D multiphase flow, multicomponent reactive transport numerical model is developed in this section to explore the methane dynamics within the thawing subsea permafrost. This model simulates 1) the top-down heat transport from the seafloor and the bottom-up heat flow from geothermal heat supply, 2) the temperature-salinity dependent ice melting, 3) the temperature-dependent organic carbon biodegradation and methanogenesis, 4) the methane transport by free gas flow and by diffusion and advection with liquid water flow, and 5) the pressure-temperature-salinity dependent methane hydrate dissociation.

2.1 Mass and energy conservation equations

There are three components (κ), methane (m), water (w) and salt (s), which can form four phases (β), liquid water (l), solid ice (i), free methane gas (v), and solid methane hydrate (h) (You & Flemings, 2018; You et al., 2019). The model assumes:

1) Thermodynamic equilibrium. This means only stable phases can be present in each corresponding pressure and temperature regime (Figure 1).

2) Gas phase is composed of methane only.

3) Ice phase is composed of water only.

4) Salt is present only in the liquid water phase.

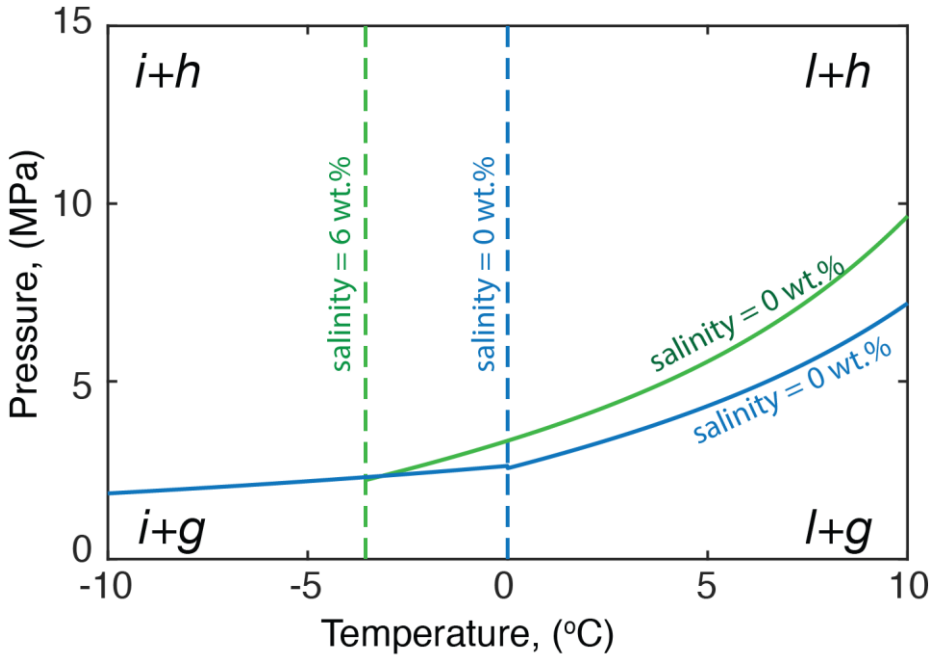

Figure 1: Phase diagram in a system with water, methane, and salt. The solid lines are the phase boundaries for methane hydrate and free methane gas at pore water salinity 0 wt.% (solid blue line) and 6 wt.% (solid green line), respectively. They are calculated using the Equations in Figure 2.1. of Moridis et al. (2008). The impact of salinity to the methane hydrate phase boundary is calculated using Equation 3 in Sun and Mohanty (2006). The dashed lines are the phase boundaries between ice and liquid water at pore water salinity 0 wt.% (dashed blue line) and 6 wt.% (dashed green line), respectively. They are calculated using Equation 3b in Sun and Mohanty (2006). 'i+h' means ice coexists with methane hydrate; 'i+g' means ice coexists with free methane gas; 'I+h' means liquid water coexists with methane hydrate; 'I+g' means liquid water coexists with free methane gas.

With these assumptions, the mass conservation equations for water (w), methane (m) and salt (s) are described by (You & Flemings, 2018; You et al., 2019):

$$\frac{\partial}{\partial t}\left[n\sum_{\beta=l,i,v,h}\rho_\beta S_\beta X_\beta^\kappa\right]+\frac{\partial}{\partial z}\left[\sum_{\beta=l,v}q_\beta\rho_\beta X_\beta^\kappa\right]-\frac{\partial}{\partial z}\left[nS_l D_l^\kappa\frac{\partial\left(\rho_l X_\beta^\kappa\right)}{\partial z}\right]-q^\kappa=0, \qquad (1)$$

where t is time (s); z is depth and is positive downward (m); ρ_β is the density (kg m^{-3}) of β phase; X_β^κ is the mass fraction of component κ in phase β (dimensionless); D_l^κ is the molecular diffusion coefficient (m^2 s^{-1}) of component κ in pore water, and $D_l^\kappa = nS_l D_{l0}^\kappa$; D_{l0}^κ is the molecular diffusion coefficient (m^2 s^{-1}) in free water; q^κ is the source or sink of component κ (kg m^{-3} s^{-1}); q_β (m^3 m^{-2} s^{-1}) is the volumetric flux of liquid water ($\beta = l$) or free gas ($\beta = v$), and is described by Darcy's law

$$q_l = -\frac{kk_{rl}}{\mu_l}\left(\frac{\partial P_l}{\partial z} - \rho_l g\right), \quad (2a)$$

$$q_v = -\frac{kk_{rv}}{\mu_v}\left(\frac{\partial P_v}{\partial z} - \rho_v g\right), \quad (2b)$$

where g is the acceleration due to gravity (m s^{-2}); μ_β and P_β are the dynamic viscosity (Pa s) and pressure (Pa) of β phase, respectively; $P_v = P_l + P_{cvl}$, and P_{cvl} is the gas-liquid water capillary pressure (Pa); k is the sediment effective permeability (m^2), permeability of the sediment to single-phase liquid water or free gas flow in presence of ice and/or methane hydrate.

Melting of ice and dissociation of methane hydrate increases the sediment effective permeability, which is described following the pore-filling model (Kleinberg et al., 2003; Kleinberg & Griffin, 2005):

$$k = k_0\left[1 - (S_i + S_h)^2 + \frac{2(1-S_h-S_i)^2}{log(S_i+S_h)}\right], \quad (3)$$

where k_0 is the sediment intrinsic permeability (m^2), permeability of the sediment to single-phase liquid water or free gas flow in absence of ice and methane hydrate; k_{rl} and k_{rv} are the relative water and gas permeability, respectively, which are calculated using the effective water ($\frac{S_l}{1-S_h-S_i}$) and gas saturation ($\frac{S_v}{1-S_h-S_i}$) (You & Flemings, 2018; You et al., 2019) and the Corey's model (Bear, 1972).

The energy conservation of the system is described by (You & Flemings, 2018; You et al., 2019)

$$\frac{\partial}{\partial t}\left[(1-n)\rho_R C_R T + \sum_{\beta=l,i,v,h} nS_\beta \rho_\beta u_\beta\right] + \frac{\partial}{\partial z}\left[\sum_{\beta=l,v} q_\beta \rho_\beta h_\beta\right] - \frac{\partial}{\partial z}\left[\lambda \frac{\partial T}{\partial z}\right] - q^e = 0. \quad (4)$$

Equation 4 includes heat transport by advection (the second term) and conduction (the third term). C_R is the heat capacity of the solid grain (J kg^{-1} K^{-1}); T is temperature (°C); u_β and h_β are the specific internal energy (J kg^{-1}) and specific enthalpy (J kg^{-1}) of β phase, respectively; q^e is the energy sink or source (J m^{-3} s^{-1}), and is described by (You & Flemings, 2018)

$$q^e = \frac{\partial(n\rho_i L_i S_i)}{\partial t} + \frac{\partial(n\rho_h L_h S_h)}{\partial t}, \quad (5)$$

to simulate the latent heat of ice melting (L_i, J kg^{-1}) and methane hydrate dissociation (L_h, J kg^{-1}). λ is the bulk thermal conductivity (W m^{-1} $°C^{-1}$), and is calculated using the parallel model (Muraoka et al., 2019; Waite et al., 2009)

$$\lambda = (1-n)\lambda_R + nS_l\lambda_l + nS_i\lambda_i + nS_v\lambda_v + nS_h\lambda_h. \quad (6)$$

In Equation 6, λ_R, λ_w, λ_i, λ_v, and λ_h are the heat conductivity (W m^{-1} K^{-1}) of solid grains, liquid water, ice, free methane gas, and methane hydrate, respectively.

2.2 Subseafloor methane sources

This model simulates two potential methane sources. The first is the dissociation of methane hydrate. The rate of methane hydrate dissociation is thermodynamic-equilibrium constrained.

The second methane source is the temperature-dependent organic carbon biodegradation. It is described by the Introductory Carbon Balance Model (ICBM) (Andrén & Kätterer, 1997). In this model, the total organic carbon falls into two pools, the labile pool with a relatively high reactivity k_1 and a stable pool with a relatively low reactivity k_2. A fraction h of the degrading material from the labile pool flows into the stable pool representing humification. The remaining part $(1-h)$ leaves the system as CH_4 and CO_2. The mass conservation equations for the labile and stable organic carbon are (Andrén & Kätterer, 1997).

$$\frac{dC_{labile}}{dt} = -k_1 r(T) C_{labile}, \quad (7a)$$

$$\frac{dC_{stable}}{dt} = hk_1 r(T) C_{labile} - k_2 r(T) C_{stable}, \quad (7b)$$

where C_{labile} and C_{stable} are the carbon content (wt.%) of the labile and stable pools, respectively; $r(T)$ is the temperature response factor, the ratio of the organic carbon reactivity at temperature T to that at a reference temperature T_{ref} (4 ^{o}C in this study). $r(T)$ is calculated by (Kätterer et al., 1998)

$$r(T) = \frac{(T-T_{min})^4}{(T_{ref}-T_{min})^4} . \quad (8)$$

With $T_{min} = -17$ ^{o}, the predictions from Equation 8 match well with the compiled data from more than 20 laboratory incubation experiments (Figure 2a) (Kätterer et al., 1998; Rivkina et al., 2002). T_{min} is the minimum temperature for biodegradation (^{o}C). Biodegradation only occurs when temperature is above T_{min}.

The microbial methane generation rate (q^m, kg m^{-3} s^{-1}) is calculated by (You & Flemings, 2021)

$$q^m = A\left[k_1 r(T)\alpha C_{org} + k_2 r(T)(1-\alpha) C_{org}\right]. \quad (9)$$

where C_{org} is the total organic carbon content (wt.%); α is the fraction of the labile organic carbon (dimensionless) with $C_{labile} = \alpha C_{org}$ and $C_{stable} = (1-\alpha)C_{org}$. A is a conversion factor and $A = 0.5 \times \frac{16}{12}\rho_R(1-n)$ (You & Flemings, 2021). Reactivities of the organic carbon (k_1, k_2) at 4 ^{o}C are obtained by fitting the model (Equations 7 and 9) to the measurements from a 7 year-long laboratory incubation experiment on permafrost soils under anoxic condition with $\alpha = 0.5\%$ and $h = 0.7$ (Figure 2b-2c) (Knoblauch et al., 2018; Knoblauch et al., 2013).

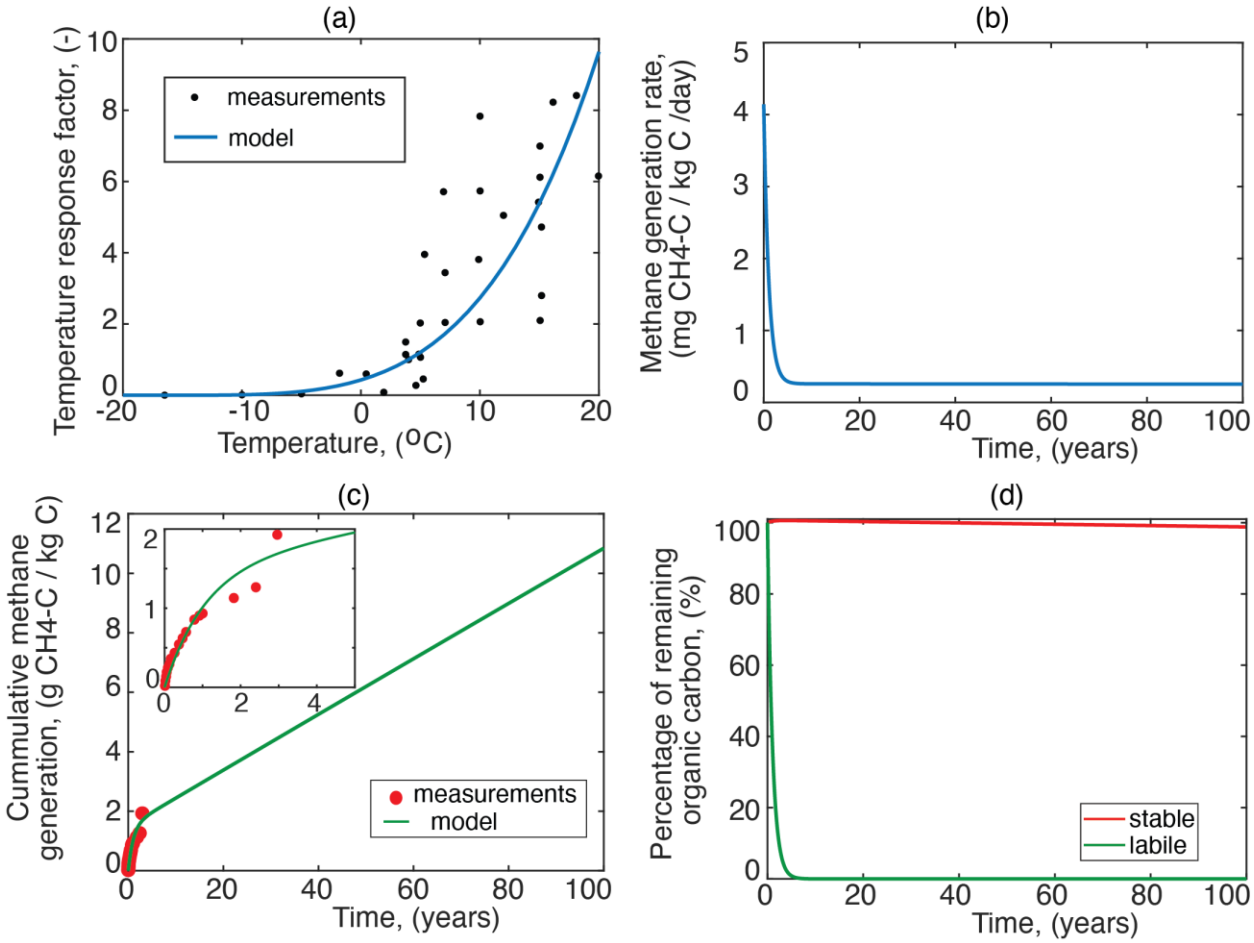

Figure 2: (a) Change of the temperature response factor ($r(T)$) from -20 ^{o}C to 20 ^{o}C with a reference temperature $T_{ref} = 4\ ^{o}C$. Temperature response factor describes the ratio of the organic carbon reactivity to the reactivity at a reference temperature. The black dots are measurements compiled by Kätterer et al. (1998) and Rivkina et al. (2002). The blue line is the prediction by Equation 8. The predicted (b) microbial methane generation rate, (c) cumulative methane generation, and (d) percentage of organic carbon remained at 4 ^{o}C using the methanogenesis model described in Equation 9 and parameters $\alpha = 0.5\%$, $h = 0.7$, $k_1 =$

$0.3 \times 10^{-7} s^{-1}$, *and* $k_2 = 0.6 \times 10^{-11} s^{-1}$ *(Knoblauch et al., 2018; Knoblauch et al., 2013). In Figure 2c, the inset shows a zoom-in view of the first 5 years, and the red dots show the measurements by Knoblauch et al. (2018). In Figure 2d, the red line shows the stable or less reactive pool of the organic carbon, and the green line shows the labile or more reactive pool of the organic carbon. The predicted methane production rate is high at the onset of biodegradation. However, as the labile organic carbon is consumed up within 8 years, the methane production rate quickly declines. Later methane production is fueled by the stable component of the organic carbon, which requires ~30 kyrs to be consumed up.*

2.3 Numerical method

The numerical model is solved by a block-centered finite-volume method (Liu & Flemings, 2007). Upstream weighting is used to calculate the phase mobility, and harmonic weighting is used to calculate the sediment effective permeability. At each timestep, the discretized mass and energy conservation equations are solved fully implicitly using the residual-based Newton Raphson method. After convergence, the methane generation rate and the remaining amount of labile and stable organic carbon are calculated for the next timestep.

3. Carbon stability in the thawing subsea permafrost

3.1 Numerical model setup

Eight different simulations are conducted to explore the evolution of the subsea permafrost and the carbon stability from 18,000 years (kyr) before present (BP) using typical parameters in the Arctic (Table 1). All simulations model a 1D domain from the ground surface/seafloor to 1200 m depth, which is discretized into 120 blocks with a vertical size 10 m. The system is at thermodynamic equilibrium before flooding. Case-1 models a system at the current day water depth 120 m. Before flooding at 18 kyrs BP, temperature equals -20 ^{o}C at the ground surface and increases linearly with depth with a geothermal heat flux 60 mW m^{-2} (Frederick & Buffett, 2014; Graw et al., 2023; Nicolsky et al., 2012; Petit et al., 1999) (Figure 3). This allows the formation of a 645 m-thick permafrost from the ground surface. Ice saturation equals 80% throughout the permafrost (Figure 4a). Salinity decreases from 22.9 wt.% at the ground surface to 3.7 wt.% at 645 m according to the temperature (Figures 1, 3c). Salinity equals 3.2 wt.% below the permafrost. Pressure equals the atmospheric pressure 0.1 MPa at the ground surface and increases hydrostatically with depth.

274 *Table 1: Input parameters for the simulations.*

Parameters and physical meanings	Values	Reference
Sediment porosity (n), dimensionless	0.35	Collett et al. (2011)
Sediment intrinsic permeability (k_0), m^2	10^{-15}	Frederick & Buffett (2014)
Residual water saturation (S_{rl}), dimensionless	0.1	You & Flemings (2021)
Residual gas saturation (S_{rv}), dimensionless	0	You et al. (2021)
Gas-liquid water capillary pressure (P_{cvl}), MPa	0.20	Liu & Flemings (2007)
Heat capacity of sediment grains (C_R), J K^{-1} kg^{-1}	730	Waite et al. (2009)
Heat capacity of methane hydrate (C_h), J K^{-1} kg^{-1}	2100	Liu & Flemings (2007)
Heat capacity of water (C_l), J K^{-1} kg^{-1}	4200	Waite et al. (2009)
Heat capacity of methane gas (C_v), J K^{-1} kg^{-1}	3500	Liu & Flemings (2007)
Heat capacity of ice (C_i), J K^{-1} kg^{-1}	2108	Frederick & Buffett (2014)
Thermal conductivity of sediment grains (λ_R), W m^{-1} K^{-1}	2.3	Wright et al. (2005)
Thermal conductivity of methane hydrate (λ_h), W m^{-1} K^{-1}	0.49	Liu & Flemings (2007)
Thermal conductivity of water (λ_l), W m^{-1} K^{-1}	0.58	Waite et al. (2009)
Thermal conductivity of methane gas (λ_v), W m^{-1} K^{-1}	0.033	Liu & Flemings (2007)
Thermal conductivity of ice (λ_i), W m^{-1} K^{-1}	2.2	Waite et al. (2009)
Density of methane hydrate (ρ_h), kg m^{-3}	912	Liu & Flemings (2007)
Density of ice (ρ_i), kg m^{-3}	917	Waite et al. (2009)
Density of solid grains (ρ_R), kg m^{-3}	2750	Liu & Flemings (2007)
Thickness of yedoma soil, m	50	Strauss et al. (2021)
Organic carbon content in Yedoma soil (C_{org}), wt.%	3.5	Zimov et al. (2006)
Organic carbon content in mineral soil (C_{org}), wt.%	1	Davie & Buffett (2001)
Fraction of labile organic carbon pool (α), %	0.5	Knoblauch et al., 2013
Fraction of stable organic carbon pool (1-α), %	99.5	Knoblauch et al., 2013
Reactivity of the labile organic carbon for Yedoma soil at 4 °C (k_1), s^{-1}	0.3×10^{-7}	Fit model to measurements in Knoblauch et al. (2018)
Reactivity of the stable organic carbon for Yedoma soil at 4 °C (k_2), s^{-1}	0.6×10^{-11}	Fit model to measurements in Knoblauch et al. (2018)
Humidification coefficient (h), dimensionless	0.7	Fit model to measurements in Knoblauch et al. (2018)
Reactivity of labile organic carbon for mineral soil at 4 °C (k_1), s^{-1}	0.3×10^{-11}	Malinverno (2010)
Reactivity of stable organic carbon for Yedoma soil at 4 °C (k_2), s^{-1}	0.6×10^{-15}	-
Minimum temperature for methanogenesis (T_{min}), °C	-17	Fit model to measurements in Katterer et al. (1998) and Rivkina et al. (2002)

Reference temperature for methanogenesis (T_{ref}), ^{o}C	4	Knoblauch et al. (2013), Knoblauch et al. (2018)
Initial permafrost layer thickness, m	650	Collett et al. (2011)
Initial ice saturation (S_i), dimensionless	0.8	Collett et al. (2011)
Initial methane hydrate saturation (S_h), dimensionless	0.5	Collett et al. (2011)
Geothermal heat flux, mW m^{-2}	60	Nicolsky et al. (2012)
Bottom water temperature, ^{o}C	-1.3	Nicolsky et al. (2012)
Bottom water salinity, wt.%	3.2	Frederick & Buffett (2014)
Latent heat of hydrate (L_h), kJ kg^{-1}	418	Liu & Flemings (2007)
Latent heat of ice melting (L_i), kJ kg^{-1}	334	Frederick & Buffett (2014)

A 50 m-thick yedoma layer is buried below the ground surface with a constant total organic carbon content 3.5 wt.% (Strauss et al., 2021; Zimov et al., 2006), of which 0.5% falls in the labile pool and has a reactivity $k_1 = 0.3 \times 10^{-7}$ s^{-1} (Table 1) (Knoblauch et al., 2018; Knoblauch et al., 2013). The rest belongs to the stale pool and has a reactivity $k_2 = 0.6 \times 10^{-11}$ s^{-1} (Table 1). The underlying mineral soil has a constant total organic carbon content 1 wt.%, typical value for the world's near seafloor sediment in deeper water (Davie & Buffett, 2001; You et al., 2021). Reactivities of the organic carbon are set to 4 orders of magnitude lower in the mineral soil than yedoma soil, which yields a reactivity value 0.3×10^{-11} s^{-1} for the labile component, typical value for deeper water marine sediments (Table 1) (Malinverno, 2010; You & Flemings, 2021).

Methane hydrate is stable from 145 m to 1045 m at 18 kyrs BP (Figure 3d). Three 30 m-thick methane hydrate deposits are buried below the ground surface with a constant hydrate saturation 50% (Figure 4b). The shallow hydrate deposit is at 195 m-225 m, near the top of the methane hydrate stability zone (MHSZ); the middle hydrate deposit is at 645 m -675 m, right below the base of the permafrost; the deep hydrate deposit is at 1015 m -1045 m, right above the base of the MHSZ (Figure 4b).

Temperature at the top of the domain is immediately increased to the bottom water temperature -1.3 ^{o}C upon flooding at 18 kyr BP (Nicolsky et al., 2012). After that temperature is kept constant at the seafloor until present (0 kyr). All simulations are extended to 2 kyrs after present to explore the future projections. Four scenarios of future warming are explored: SSP1-2.6 (Case-2), SSP2-4.5 (Case-1), and SSP5-8.5 (Case-3) from the Max Planck Institute Earth System Model runs (Kleinen et al., 2021) and no further warming in the future (Case-4). In

SSP1-2.6 (Case-2), SSP2-4.5 (Case-1), and SSP5-8.5 (Case-3), seabed temperature is increased linearly by 1 ^{o}C in the next 100 years, 2 ^{o}C in the next 100 years and 8 ^{o}C in the next 400 years, respectively, and then kept constant. In Case-4 seabed temperature is constant (-1.3 ^{o}C) from 18 kyrs BP to 2 kyrs after present.

With the linear rising of water depth from 0 m at 18 kyr BP to 120 m at present, the pressure at the seabed increases accordingly (Frederick & Buffett, 2014; Kendall et al., 2005). The same sea level rising rate is maintained for the next 2 kyrs for simplification. There is constant geothermal heat supply (60 mW m^{-2}) and no fluid flow and mass transport at the bottom of the model (Graw et al., 2023; Nicolsky et al., 2012).

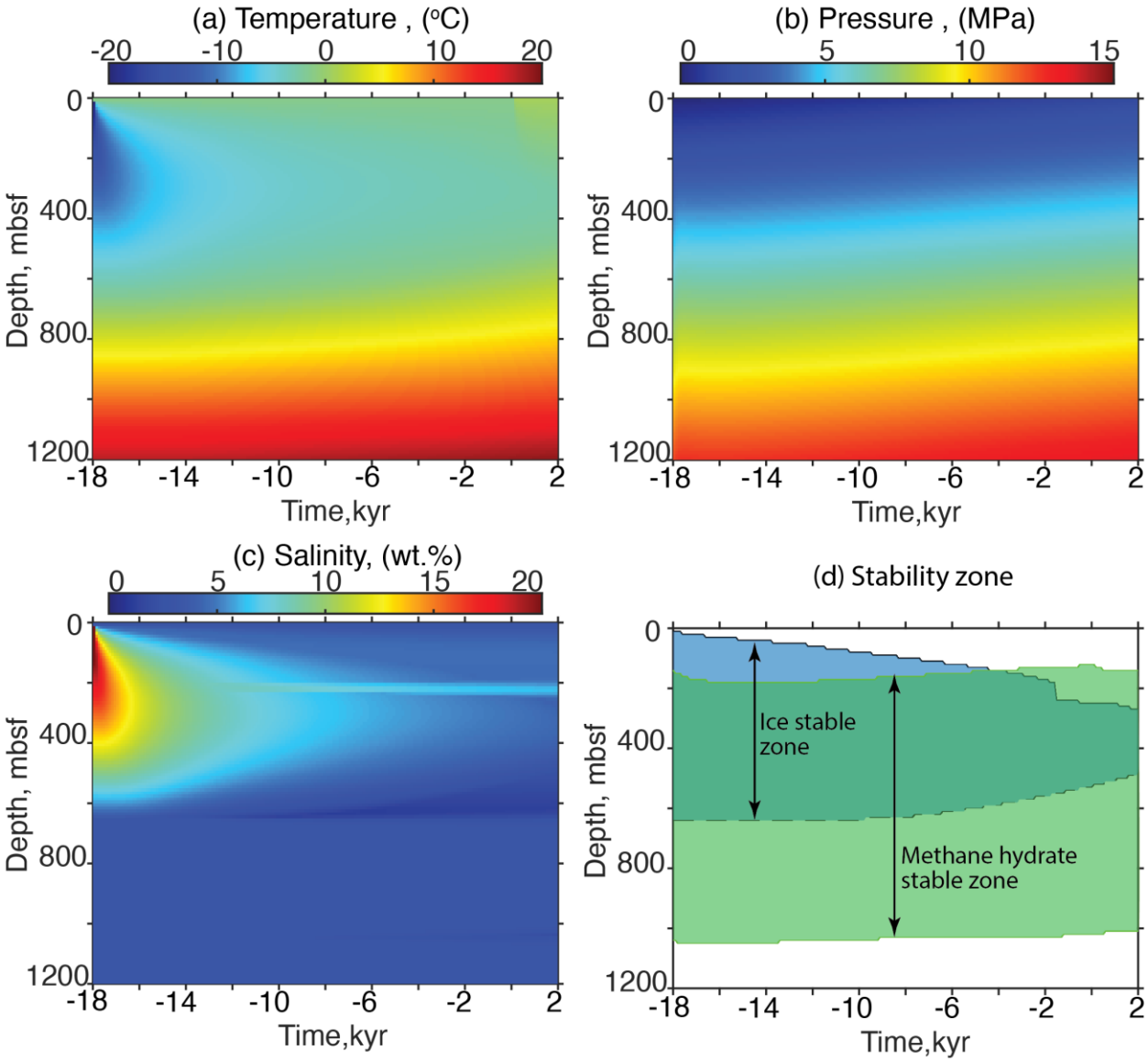

Figure 3: Case-1: Evolution of (a) temperature, (b) pore water pressure, (c) pore water salinity and (d) ice (blue) and methane hydrate stability zone (green) following the flooding at 18,000 years (18 kyrs) before present. Negative values for horizontal axis mean time before present, '0' means present, and positive values mean time into the future. 'mbsf" means meter below seafloor.

3.2 Modeling results

Following the flooding at 18 kyrs BP, temperature gradually increases in the sediment (Figure 3a, Supporting Information). The top-down warming drives ice to melt and permafrost to retreat from the seafloor (Figure 4a), which releases fresh water and decreases the local salinity (Figure 3c). A decreasing salinity means a higher temperature is required to melt the remaining ice (Figure 1). Heat conduction from the seabed reverses the temperature gradient in the shallow sediment (Figure 3a). This causes the accumulation of the geothermal heat within the permafrost and drives ice melting from the base of the permafrost from 4 kyrs following the flooding (Figure 4a). The thickness of the permafrost shrinks to 290 m at present, extending from 245 m to 535 m below the seafloor (Figure 4a). The average ice saturation declines from 80% before inundation to 24% at present (Figure 4a).

In contrast, the MHSZ stays nearly constant throughout the simulation, with both its top and bottom slightly moving up (Figure 3d: green color). Methane hydrate is quite stable in the shallow and middle hydrate layers where the methane hydrate maintains the initial saturation (50%) (Figure 4b). Methane hydrate does dissociate in the deep deposit, starting from 9 kyrs BP (Figure 4b). However, the released methane gas does not reach the seafloor. Instead, it is trapped at the new base of the MHSZ as newly formed methane hydrate (Figure 4b).

When temperature increases to above -17 ^{o}C, methanogenesis immediately starts in the yedoma layer (Figure 5). It is fueled by biodegradation of the organic carbon near the seafloor (Figure 5a). The labile component is consumed up in the entire yedoma layer after 300 years' biodegradation (Figure 5a). After that methanogenesis is sustained by the stable component of the organic carbon (Figure 5b). The rate of methane production increases initially following the flooding with the rising temperature (Figure 5c). The rate starts declining at ~4 kyrs following the flooding as the remaining amount of organic carbon decreases (Figure 5c).

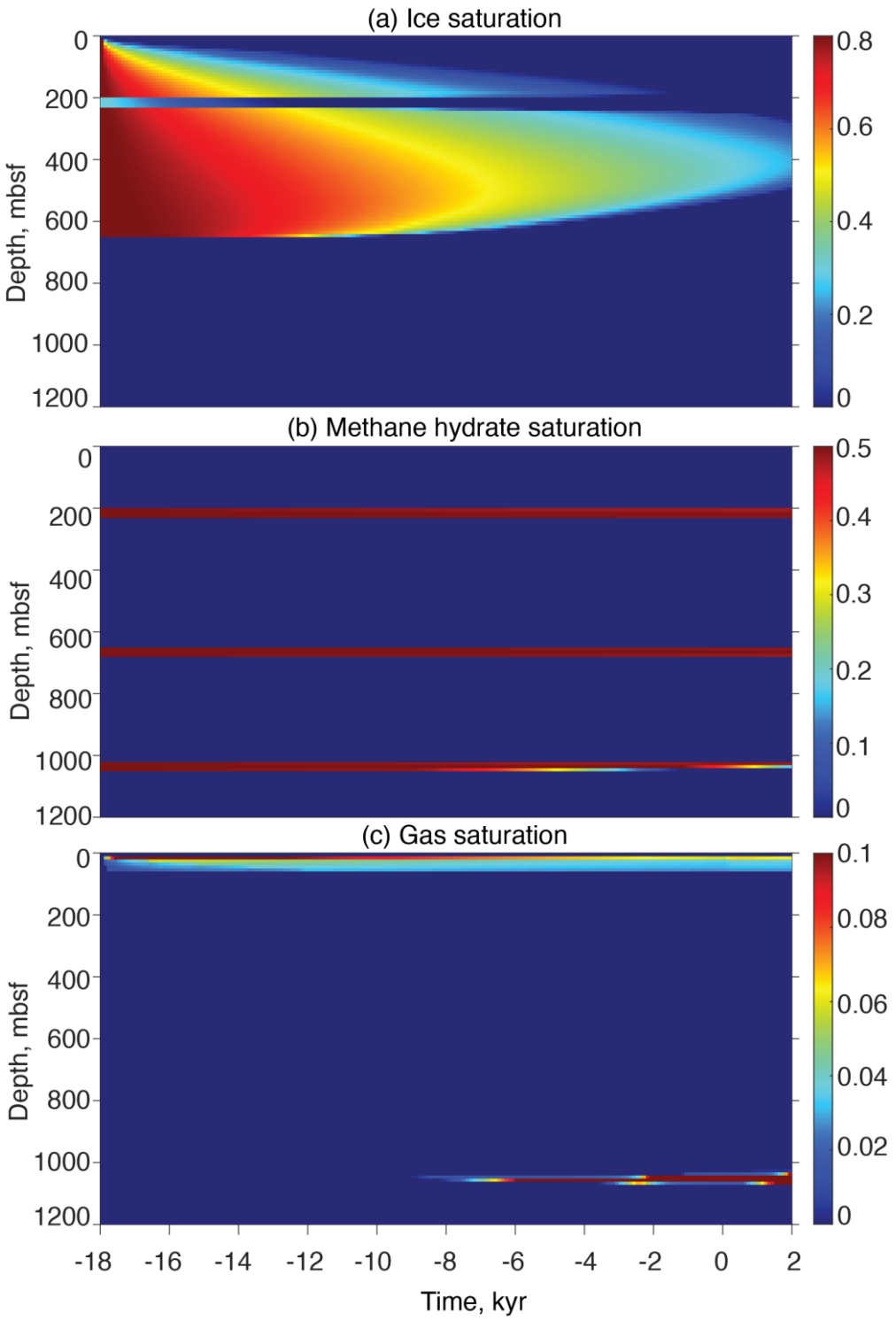

Figure 4: Case-1: Evolution of (a) ice saturation, (b) methane hydrate saturation, and (c) gas saturation following the flooding at 18,000 years (18 kyrs) before present. Horizontal axis has the same meaning as Figure 3.

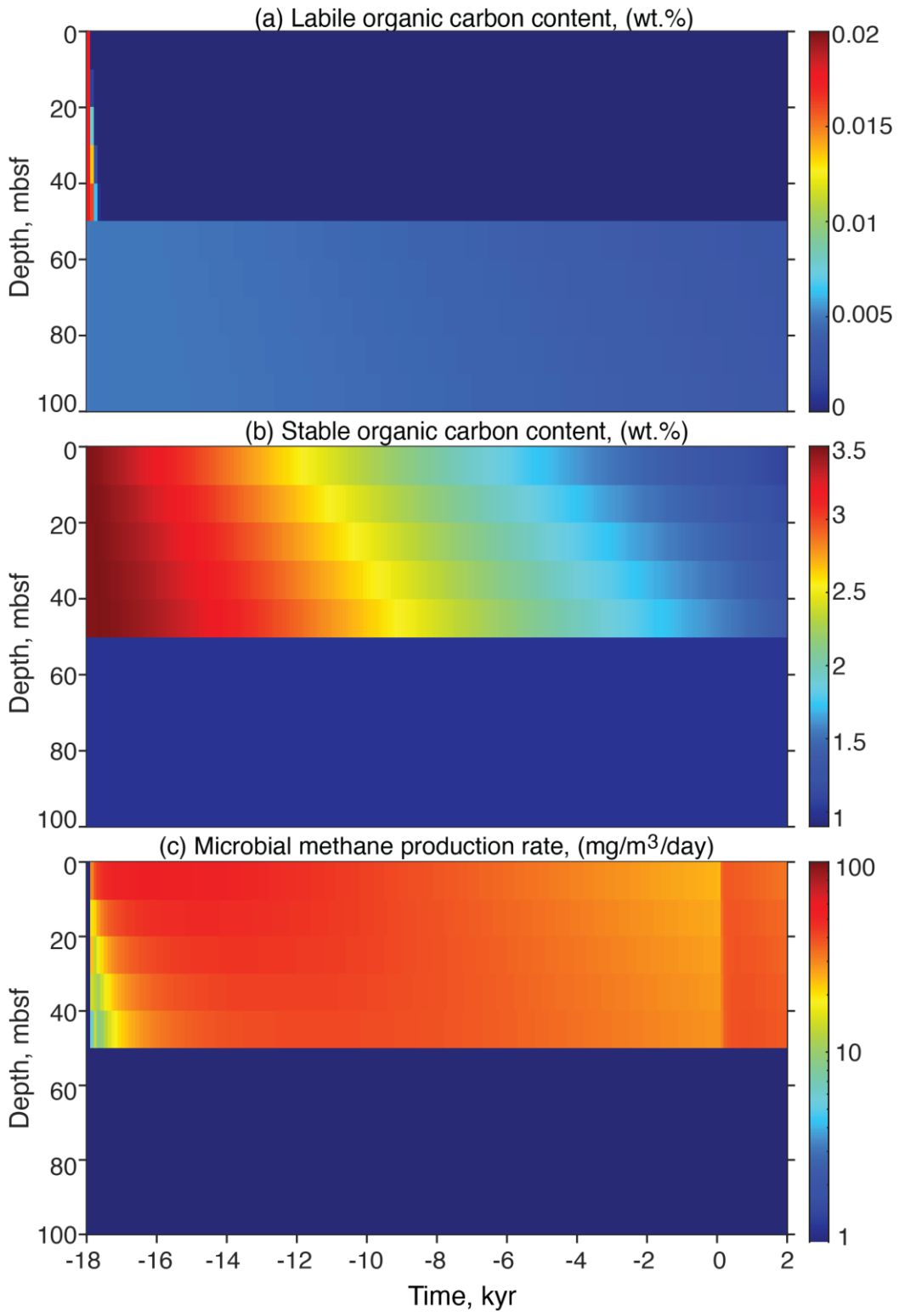

341

342 *Figure 5: Case-1: Evolution of (a) labile organic carbon content, (b) stable organic carbon*
343 *content, and (c) gas saturation following the flooding at 18,000 years (18 kyrs) before present.*
344 *Horizontal axis has the same meaning as Figure 3.*

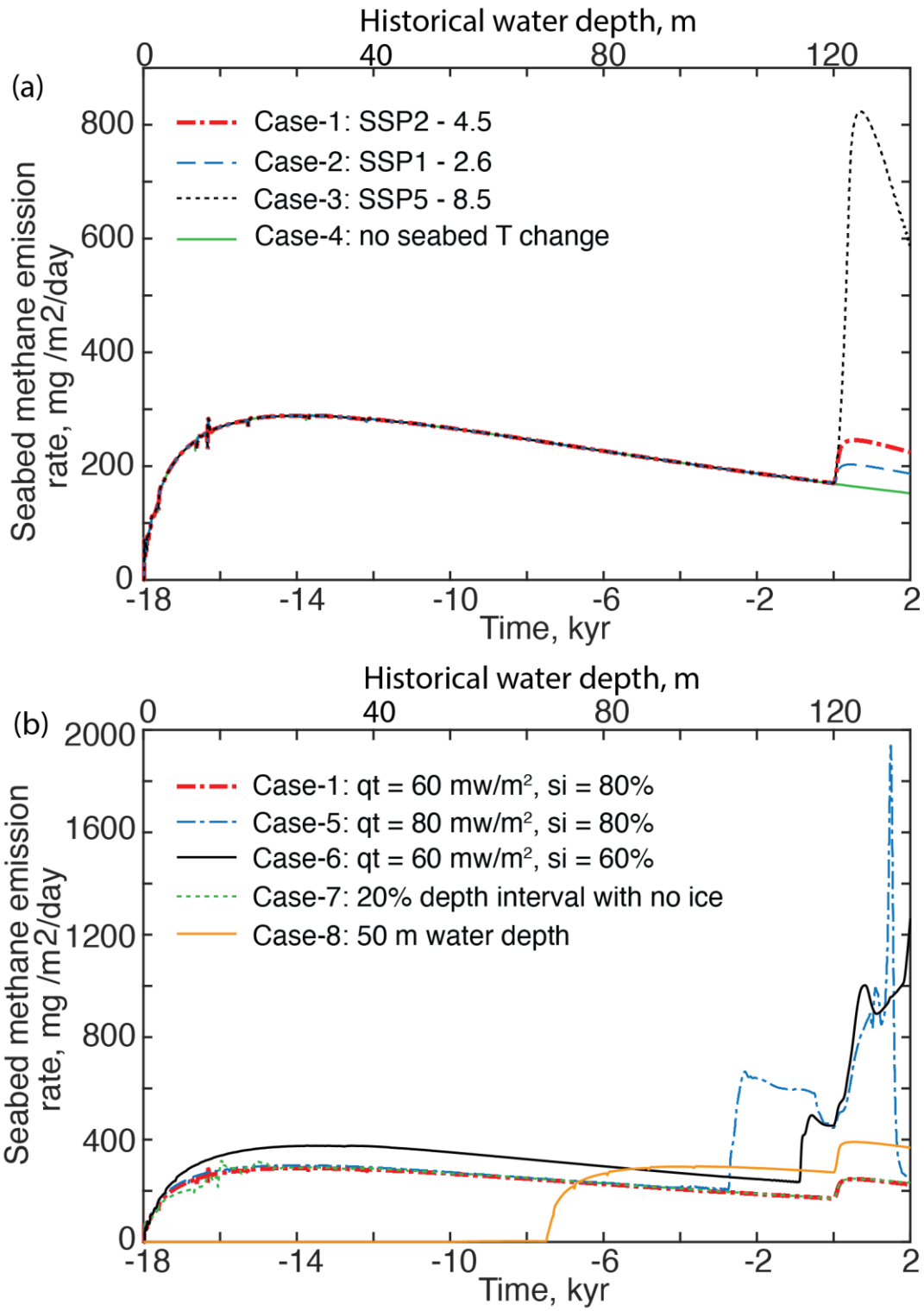

345

346 *Figure 6: Evolution of seabed methane emission rate following the flooding at 18,000 years (18*
347 *kyrs) before present. Horizontal axis has the same meaning as Figure 3.*

Seabed methane emission starts immediately (25 years) following the flooding and lasts for the rest of the simulation period (Figure 6a). The seabed methane emission is in the form of free gas flow (Figure 4c). It is fueled by biodegradation of the organic carbon in the yedoma layer. The methane flux increases initially as the methanogenesis rate increases throughout the yedoma layer (Figure 6a). It reaches a peak value 288 mg m^{-2} day^{-1} at 4 kyrs following the inundation when the subseafloor methanogenesis rate is highest. The seabed methane flux drops to 172 mg m^{-2} day^{-1} at present (Figure 6a).

If there is no further warming in the future (Case-4), the seabed methane flux continues decreasing in the next 2 kyrs (Figure 6a: green line). However, further warming in the future further increases the sediment temperature near the seafloor (Figure 3a). This increases the reactivity of the remaining organic carbon, enhances the methanogenesis and amplifies the seabed methane emission (Figure 6a: blue, red and black lines). If the future warming magnitude is less than 2 ^{o}C (Case-1, 2, 4), the maximum seabed methane emission is less than 250 mg m^{-2} day^{-1} and is solely fueled by biodegradation of the organic carbon in the yedoma layer. However, a higher magnitude warming in scenario SSP5-8.5 (Case-3) elevates the seabed methane flux to 823 mg m^{-2} day^{-1} at 672 years after present (Figure 6a: black line). This is 4 times the current day seabed microbial methane flux. In addition, such a high magnitude warming causes methane hydrate to start dissociating in the shallow deposit from 1.4 kyrs after present, which significantly increases the seabed methane flux when the released gas reaches the seafloor.

Case-5 simulates a higher geothermal heat flux, 80 mW m^{-2}, compared with Case-1 (Figure 7, Supporting Information). The thickness of the permafrost reduces to 485 m at thermodynamic equilibrium at 18 kyrs BP (Figure 7). The base of the MHSZ moves up to 715 m (Figure 7a: green color). The middle and the deep methane hydrate deposits are moved up to 485-515 m and 695-715 m, respectively, to accommodate the new thermodynamic condition (Figure 7c). A higher geothermal heat flux drives faster ice melting from the base of the permafrost (Figure 7b). Permafrost disappears from the entire sediment at ~5 kyrs BP (13 kyr following the flooding) (Figure 7b). In addition, the higher geothermal heat flux drives earlier and faster methane hydrate dissociation from both the shallow and the deep hydrate deposits (Figure 7c). Methane hydrate starts dissociating from the shallow hydrate deposit at 4 kyrs BP (Figure 7c). The released free methane gas reaches the seafloor and starts venting methane into the seawater from 2 kyrs BP (Figure 7d). Before that the seabed methane emission is solely

fueled by microbial methanogenesis and has a same low flux as Case-1 (Figure 6b: blue line). The addition of the methane from the dissociating methane hydrate dramatically increases the seabed methane flux. The seabed methane flux jumps to 665 mg m^{-2} day^{-1} at 2.3 kyrs BP, 3.5 times of the flux fueled by microbial methanogenesis only (Figure 6b: compare the blue and the red curves). A 2 ^{o}C rise of the seabed temperature in the next 100 years (SSP2-4.5) further amplifies the seabed methane flux. The seabed methane flux further jumps to 1937 mg m^{-2} day^{-1} at 1.4 kyrs after present, more than 10 times the flux fueled by biodegradation only (Figure 6b: blue line). This further rise of methane flux is caused by the accelerated dissociation of methane hydrate in the shallow deposit. The shallow methane hydrate deposit is exhausted at 1.4 kyrs after present, after which the seabed methane flux drops rapidly to the flux sourced from biodegradation only (Figure 6b: blue line).

In Case-6 (Supporting Information), ice saturation is reduced to 60% throughout the 645 m-thick permafrost, compared with Case-1. A lower amount of ice means less heat is required to melt the in-situ ice. As a result, temperature rises faster in the sediment. This results in a higher microbial methanogenesis rate and a larger seabed microbial methane flux in Case-6 than Case-1 (Figure 6b: the black line is above the red line). In addition, methane hydrate starts dissociating in the shallow deposit and feeding the seabed methane emission at 880 years BP. This rapidly elevates the seabed methane flux to more than 2 times the flux fueled by biodegradation only (Figure 6b: black line). A 2 ^{o}C warming in the next 100 years (SSP2-4.5) further enhances methane hydrate dissociation and amplifies the seabed methane flux (Figure 6b: black line).

Case-7 simulates a discontinuous permafrost where a 10 m-thick ice-free interval is interbedded with a 40 m-thick ice-bearing interval for every 50 m-thick permafrost (Supporting Information). Such an ice distribution has been observed from well log data previously (Ruppel et al., 2016). Case-7 predicts a similar seabed methane flux as Case-1 (Figure 6b: green line). The seabed methane emission is fueled solely by biodegradation of the organic carbon in the yedoma deposit. Different from Case-1, the permafrost retreats much faster and disappears at 300 years after present in Case-6.

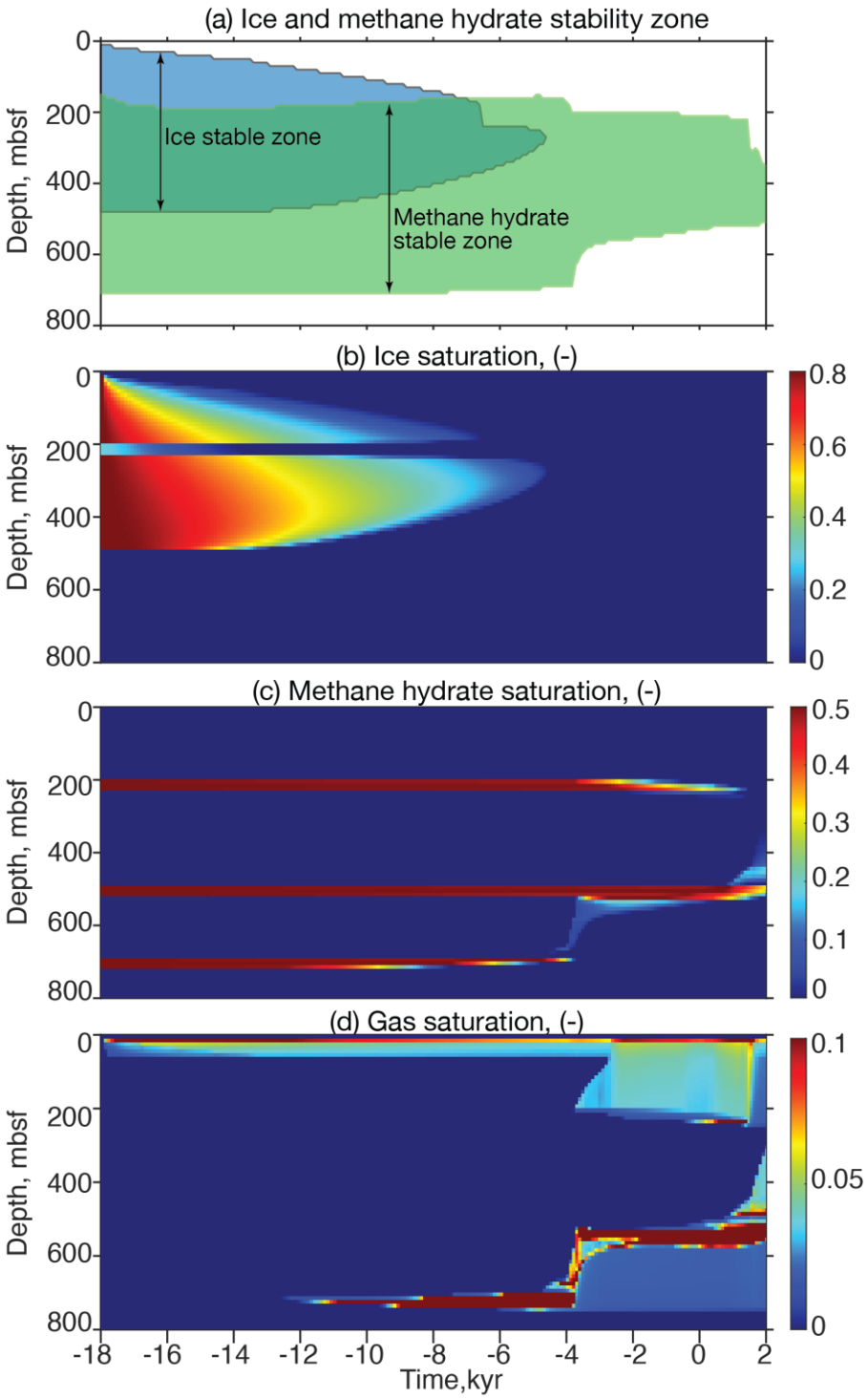

406

407 *Figure 7: Case-5 (higher geothermal heat flux): Evolution of (a) ice and methane hydrate*
408 *stability zone, (b) ice saturation, (c) methane hydrate saturation, and (d) gas saturation*
409 *following the flooding at 18,000 years (18 kyrs) before present. Horizontal axis has the same*
410 *meaning as Figure 3. Compared with Case-1, Case-5 has a higher geothermal heat flux 80 mW*
411 *m^{-2}.*

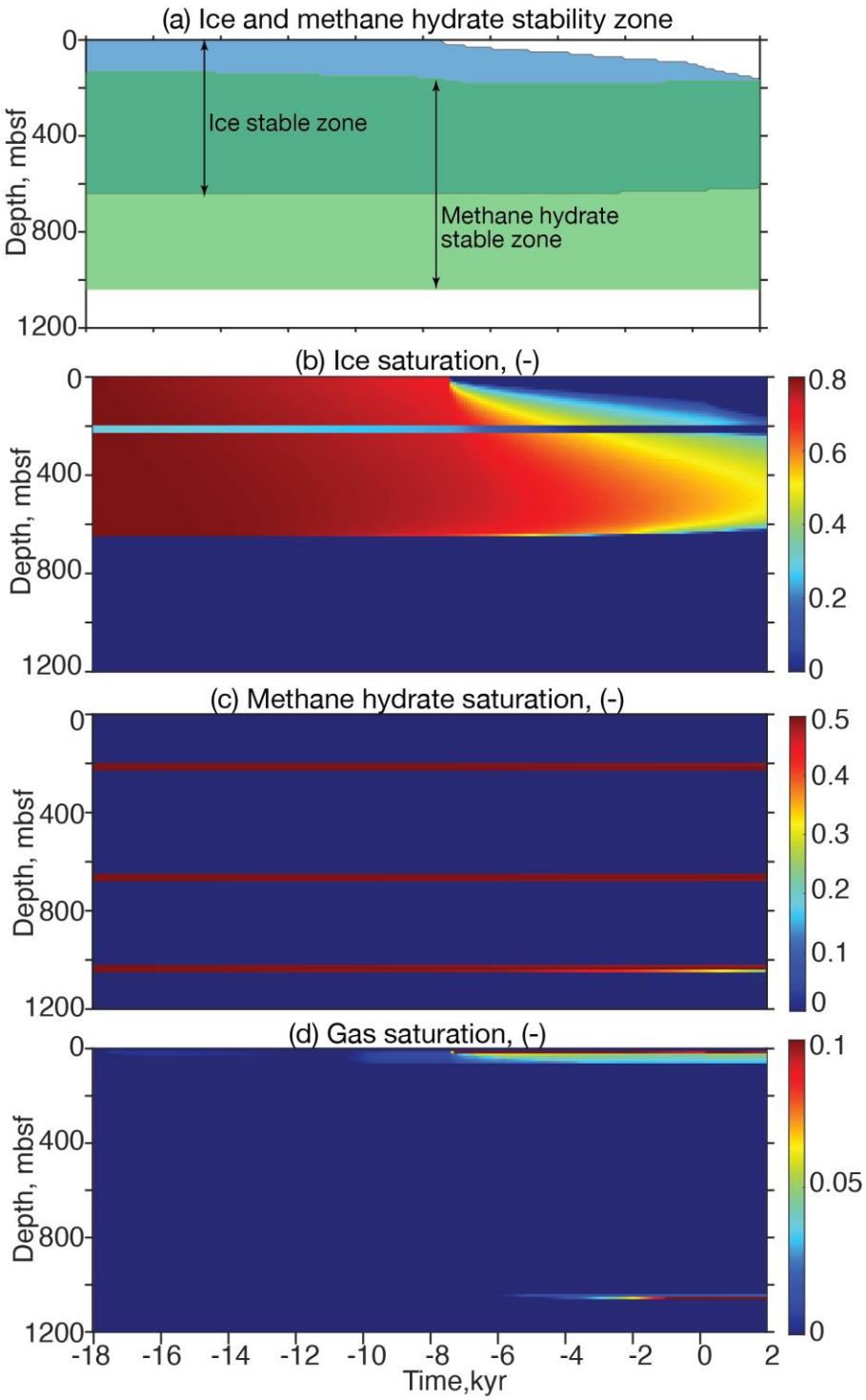

412

413 *Figure 8: Case-8 (50 m water depth): Evolution of (a) ice and methane hydrate stability zone,*
414 *(b) ice saturation, (c) methane hydrate saturation, and (d) gas saturation following the flooding*
415 *at 18,000 years (18 kyrs) before present. Horizontal axis has the same meaning as Figure 3.*
416 *Case-8 simulates the system evolution at the current water depth 50 m.*

417

Case-8 simulates the permafrost evolution at the current day water depth 50 m (Figure 8, Supporting Information). This water depth was flooded at ~7.5 kyrs BP (Figure 8) (Frederick & Buffett, 2014; Kendall et al., 2005). Before flooding, temperature at the ground surface increases linearly with time from -20 ^{o}C at 18 kyr BP to -13 ^{o}C at 10.5 kyrs BP (Frederick & Buffett, 2014; Petit et al., 1999). During this period, the temperature in the shallow sediment is not high enough to support a fast methanogenesis and allow seabed methane bubbling (Figure 8c). Thus, the seabed methane flux is negligibly low during this period (Figure 6b: orange line). Upon flooding at 7.5 kyrs BP, temperature at the top is immediately increased to -1.3 ^{o}C as Case-1. The system starts evolving similarly as the 120 m water depth (Case-1) (Figure 6b: orange line). Methane is emitted to the seawater through free gas flow. The seabed methane bubbling is fueled solely by biodegradation of the organic carbon in the yedoma layer. A thick permafrost persists until present, extending from 95 m to 635 m depth with an average ice saturation 42% (Case-8) (Figure 8).

4. Discussion

4.1. Biodegradation of the ancient organic carbon as a source of seabed methane emission

Biodegradation of organic carbon produces a seabed methane flux on the order of tens of g m^{-2} $year^{-1}$ (Figure 6). The predicted seabed methane flux is similar to the observed methane ebullition rate onshore Alaska above thermokarst lakes (Walter Anthony et al., 2016). This methane emission has a much lower magnitude but lasts much longer than fueled by methane hydrate dissociation (Figure 6).

The predicted seabed methane emission is mainly fueled by biodegradation of the organic carbon at the Arctic continental shelves. The recent sea level transgression warms and melts the inundated permafrost, reactivates the methanogenesis and causes seabed methane emission (Figure 6, Figure 9). The seabed methane emission starts immediately following the flooding and persists since then (Figure 6). This increases the dissolved methane concentration and results in methane supersaturation in the bottom water observed at the Arctic continental shelves (e.g., the East Siberian Arctic Shelf, the Beaufort Sea shelf, the Kara Sea) (Kvenvolden et al., 1993; Lorenson et al., 2016; Shakhova, Semiletov, Salyuk, et al., 2010; Shakhova et al., 2015). Other sources of methane, such as coastal riverine input, coastal erosion and submarine groundwater discharge, have also been suggested bringing methane from inland swamps and tundra

environments into the shelf water (Cramer & Franke, 2005; Sapart et al., 2017; Shakhova et al., 2015). However, the observed vigorous bubbling events at the seabed, the spatial overlap between the seabed gas bubbling and the subsea permafrost degradation, and the Pleistocene-aged or older microbial methane measured in the bottom water all suggest that a large fraction of the methane in the bottom water originates from the thawing subsea permafrost (Cramer & Franke, 2005; Lorenson et al., 2016; Pohlman et al., 2017; Sparrow et al., 2018; Steinbach et al., 2021). This same methane source has been measured fueling the widespread methane bubbling above the thermokarst lakes onshore Alaska and Siberia (Walter Anthony et al., 2016; Walter Anthony et al., 2021; Zimov et al., 1997).

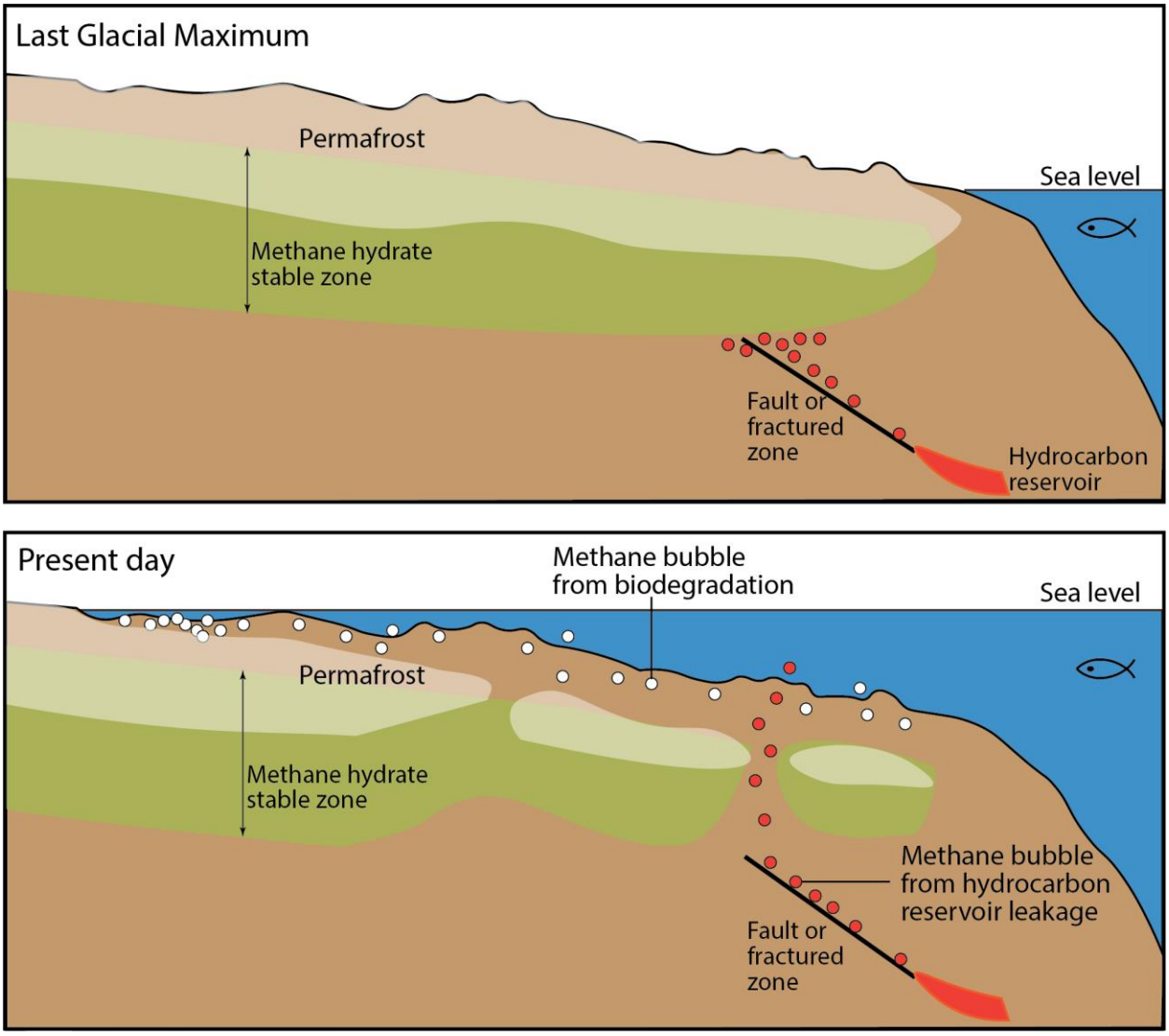

Figure 9: At Last Glacial Maximum when the sea level was ~120 m lower, large area of the current day Arctic continental shelf was exposed to extremely cold atmospheric air. Thick layers

of permafrost and methane hydrate stability zone developed below the ground surface. Post-Last Glacial Maximum sea level rise gradually flooded the permafrost and melted the ice. Biodegradation of ancient organic carbon in the thawing permafrost produces methane. The methane could eventually be emitted to the seawater by free gas flow. The predicted highest seabed microbial methane flux is in shallow water where the sediment has been warmed up, but the remaining amount of organic carbon is still high. The melting of permafrost may allow deep hydrocarbon leakage into the seawater due to the disintegration of the "cryosphere cap".

More importantly, the seabed microbial methane flux is predicted reaching its peak value shortly (~ 4 kyrs) after the flooding when water above the simulation location is still shallow (~27 m) (Figure 6). After that the seabed methane flux declines with time with the decrease of the organic carbon content in the yedoma layer. This indicates that the highest seabed microbial methane flux should be in the near shore area where the sediment has been warmed up, but the remaining amount of organic carbon is still high. Such prediction matches the observed hotspots of bottom water dissolved methane, located near the coast of the Laptev Sea, East Siberian Arctic Sea and Beaufort Sea (Chuvilin et al., 2022; Lorenson et al., 2016; Shakhova, Semiletov, Salyuk, et al., 2010; Shakhova et al., 2015). This further indicates that the bottom water methane comes from biodegradation of the previously frozen organic carbon in the thawing permafrost. Similar observations have been made onshore Alaska: hotspot methane bubbling are mostly found in the newly expanded regions of thermokarst lakes (Walter Anthony et al., 2021).

Biodegradation as the bottom water methane source indicates that not much of the released methane will reach the surface water and the atmosphere. The low-magnitude biodegradation (Figures 5c, 6) means that a large fraction of the generated methane could be consumed by the sulfate-riven AOM below the seafloor and the aerobic methane oxidation in the water column as the methane flows upward (Hong et al., 2016; Overduin et al., 2015; Ruppel & Kessler, 2017; Sparrow et al., 2018; Stranne et al., 2019). In addition, along the flow path, methane in bubbles gradually dissolves into the seawater (McGinnis et al., 2006; Ruppel & Kessler, 2017; Wang et al., 2020). Atmospheric gases (dissolved nitrogen, oxygen, argon and carbon dioxide) in the seawater gradually absorb to gas bubbles. Even in cases where gas bubbles reach the surface water, they may only contain atmospheric gases and no methane (McGinnis et al., 2006). For example, McGinnis et al. (2006) predicted that for 50% of methane contained in bubbles at the seafloor to reach the atmosphere requires minimum 10 mm diameter bubbles to be emitted at 30 m water depth. Bubble sizes measured to date are mostly less than 10

493 mm diameter (Römer et al., 2012; Skarke et al., 2014; Wang et al., 2020; Wang et al., 2016).
494 Therefore, the thawing subsea permafrost may not contribute much methane into the surface
495 water and the atmosphere. Such an inference is also supported by field measurements. Analysis
496 of water samples collected at the U.S. Beaufort Sea shelf show that although ancient carbon is
497 being mobilized and emitted as methane into the bottom water, methane in surface water is
498 principally derived from modern-aged carbon (Sparrow et al., 2018).

499 *4.2. Is methane hydrate dissociation a source of seabed methane emission?*

500 In most simulated cases (Case-1, 2, 3, 4, 7, 8), the stability zone of methane hydrate stays
501 nearly unchanged throughout the entire simulation period. All three methane hydrate deposits are
502 predicted containing methane hydrate at the original saturation until present day. This is caused
503 by three factors. First, ice melting is an endothermal process. The melting of ice in the shallow
504 sediment buffers heat transport into the hydrate deposits. Second, ice melting releases fresh
505 water and decreases salinity. The fresher pore water shifts the methane hydrate phase boundary
506 toward higher temperature, making methane hydrate more stable. Freshwater seepage has been
507 detected at the continental shelves of the Laptev Sea (Kravchishina et al., 2021) and Canadian
508 Beaufort Sea (Gwiazda et al., 2018). Third, pore water pressure increases with the rising sea
509 level. A higher pressure moves the methane hydrate phase boundary toward higher temperature,
510 especially at low temperature where methane hydrate stability is more sensitive to pressure
511 (Figure 1).
512 In rare cases (Case-5 and 6), methane hydrate dissociates and vent free methane gas to
513 the seawater. When this happens, the seabed methane flux is much higher than from the
514 biodegradation alone (Figure 6b: the black and blue lines). However, the occurrence of seabed
515 methane emission from methane hydrate dissociation is problematic. Such situation requires the
516 presence of very shallow (~200 m depth), intra-permafrost methane hydrate deposits, the
517 occurrence of which is very limited. There is only one documented case of intra-permafrost
518 methane hydrate in literature now, at ~20 km west of the Mallik, Northwest of Canada
519 (Dallimore & Collett, 2005). Formation of concentrated methane hydrate deposit requires large
520 amount of methane. In deeper-water marine sediments, three-dimensional free gas flow is
521 inferenced to focus the basin-wide microbial methane into the hydrate reservoirs (You et al.,
522 2019; You et al., 2021). In permafrost region, nearly all methane hydrate deposits discovered

nowadays is below the base of permafrost (Collett et al., 2011). Methane in those reservoirs is thermogenic and transported from deep hydrocarbon reservoirs by free gas flow along faults (Collett et al., 2011). Both cases require free gas flow, which is challenging through the ice-bearing sediment.

Besides, a high geothermal heat flux is required to dissociate methane hydrate and vent the released methane gas to the seawater. Case-5 uses a very high geothermal heat flux, 80 mW m^{-2}. Such a high geothermal heat flux is not common at the Arctic continental shelves but may occur at locations with high-rate upward fluid flow (Graw et al., 2023). Thermogenic gas seeps are widely observed at the outer shelves of the Laptev Sea and the East Siberian Arctic Sea (Baranov et al., 2020). Their formation has been attributed to the flooding-induced methane hydrate dissociation (Baranov et al., 2020; Cramer & Franke, 2005; Dmitrenko et al., 2011; Sapart et al., 2017; Sergienko et al., 2012; Steinbach et al., 2021). However, those gas seeps are directly above junctions of faults that connect to deeper hydrocarbon reservoirs (Baranov et al., 2020). They are more likely to represent the leakage of deep hydrocarbon reservoirs, like those widely observed along boundaries of permafrost thaw and melting glaciers in the terrestrial Arctic (Walter Anthony et al., 2012) and in ice-free deep-water environments (e.g., northern Gulf of Mexico) (Boyd et al., 2011; Smith et al., 2014) (Figure 9).

Case-6 also predicts seabed methane emission fueled by methane hydrate dissociation. However, besides the presence of very shallow hydrate deposit, Case-6 simulates a low initial ice saturation, 60%. At the LGM when the atmospheric temperature is less than -20 ^{o}C in the Arctic, the predicted ice saturation is nearly 100% throughout the permafrost (Frederick & Buffett, 2014).

5. Summary and conclusion

Arctic permafrost stores significant amount of carbon in frozen ancient organic carbon, solid methane hydrates and natural gas reservoirs. When sea level starts rising sharply since the LGM, a large fraction of this carbon is inundated under the much warmer seawater. This study explores the stability of the carbon pools in the Arctic permafrost following the flooding since the LGM. Eight different 1D simulations are conducted using a newly developed numerical model that fully couples the thermal, hydrological, chemical, and microbial processes occurring

within the thawing permafrost. All simulations start from 18 kyrs BP and end at 2 kyrs after present. The following conclusions can be obtained from this study:

1. Microbial methane is produced and vented at the seabed immediately upon flooding of the Arctic continental shelves. This microbial methane is generated by biodegradation of the previously frozen organic carbon in the yedoma layer near the seafloor. Flooding causes heat to be transported from the warm seawater to the cold sediment, elevates the temperature and melts the ice, which dramatically increases the reactivity of the organic carbon and enhances microbial methanogenesis.

2. The flux of seabed microbial methane emission reaches its peak value shortly following the flooding and then declines with the consumption of the organic carbon. This indicates that the highest seabed microbial methane flux is in the near shore area where the sediment has been warmed up, but the remaining amount of organic carbon is still high.

3. Without further warming in the future, the seabed microbial methane flux at deeper water depth (e.g., > 30 m) is decreasing today and in the future. However, further warming in the future could further increase the seabed methane flux to a peak value that is several times the current day flux.

4. It is less likely for methane hydrate dissociation to fuel a seabed methane emission at the Arctic continental shelves. That is because this requires the presence of very shallow, intra-permafrost methane hydrate deposit and a high geothermal heat flux. Their widespread occurrence is questionable.

Nomenclature

Superscript

e	energy
m	methane
s	salt
w	water
κ	components index

Subscript

h	hydrate phase
i	ice phase
l	liquid phase
R	solid grain
v	gas phase
β	phases index
A	conversion factor in methanogenesis model (kg m^{-3})
C_{labile}	labile organic carbon content (wt.%)
C_{org}	total organic carbon content (wt.%)
C_{stable}	stable organic carbon content (wt.%)
C_β	heat capacity of β phase (J kg^{-1} K^{-1})
D_l^κ	molecular diffusion coefficient of component κ in sediment (m^2 s^{-1})
D_{l0}^κ	molecular diffusion coefficient of component κ in free water (m^2 s^{-1})
g	acceleration due to gravity (m s^{-2})
h	humification factor (dimensionless)
h_β	specific enthalpy of phase β (J kg^{-1})
k	sediment effective permeability (m^2)
k_0	sediment intrinsic permeability (m^2)
k_1	reactivity of the labile organic carbon (s^{-1})
k_2	reactivity of the stable organic carbon (s^{-1})
k_{rl}	relative permeability of liquid water phase (dimensionless)
k_{rv}	relative permeability of free methane gas (dimensionless)
L_h	latent heat of hydrate formation and dissociation (J kg^{-1})
L_i	latent heat of ice formation and melting (J kg^{-1})
n	porosity (dimensionless)
P_{cvl}	gas-liquid water capillary pressure (Pa)
P_e	pressure at the quadruple point (Pa)
P_β	pressure of β phase (kg m^{-1} s^{-2})
q^e	energy generation rate (J m^{-3} s^{-1})

q^{κ}	sources or sinks of component κ (kg m^{-2} s^{-1})
q_{β}	volumetric flux of β phase (m^3 m^{-2} s^{-1})
$r(T)$	temperature response factor for methanogenesis model (dimensionless)
S_{rl}	residual liquid water saturation (dimensionless)
S_{rv}	residual gas saturation (dimensionless)
S_{β}	saturation of β phase (dimensionless)
t	time (s)
T	temperature (^{o}C)
T_{min}	minimum temperature below which methanogenesis stops (^{o}C)
T_{ref}	reference temperature for methanogenesis model (^{o}C)
z	depth below the ground surface/seafloor (m)
α	fraction of the labile organic carbon in the total organic carbon pool (dimensionless)
u_{β}	specific internal energy of phase β (J kg^{-1})
X_{β}^{κ}	mass fraction of component κ in phase β (dimensionless)
ρ_{β}	density of β phase (kg m^{-3})
μ_{β}	dynamic viscosity of β phase (kg m^{-1} s^{-1})
λ	bulk thermal conductivity of the porous media (W m^{-1} $^oC^{-1}$)
λ_{β}	thermal conductivity of phase β (W m^{-1} $^oC^{-1}$)

Data Availability Statement

Data used in this study are listed in Table 1.

Acknowledgements

This project is supported by the US Natural Science Foundation Office of Polar Programs (OPP) with Award #2317541. The author thanks the support from Institute for Geophysics the University of Texas at Austin.

References

Andrén, O., & Kätterer, T. (1997). ICBM: the introductory carbon balance model for exploration of soil carbon balances *Ecological Applications, 7*(4), 1226-1236. https://doi.org/https://doi.org/10.1890/1051-0761(1997)007[1226:ITICBM]2.0.CO;2

Baranov, B. V., Galkin, S., Vedenin, A., Dozorova, K., Gebruk, A., & Flint, M. V. (2020). Methane seeps on the outer shelf of the Laptev Sea: characteristic features, structural control, and benthic fauna. *Geo-Marine Letters, 40*(4), 541-557. https://doi.org/10.1007/s00367-020-00655-7

Bear, J. (1972). *Dynamics of Fluids in Porous Media*. Dover.

Berchet, A., Bousquet, P., Pison, I., Locatelli, R., Chevallier, F., Paris, J.-D., Dlugokencky, E. J., Laurila, T., Hatakka, J., Viisanen, Y., Worthy, D. E. J., Nisbet, E., Fisher, R., France, J., Lowry, D., Ivakhov, V., & Hermansen, O. (2016). Atmospheric constraints on the methane emissions from the East Siberian Shelf. *Atmos. Chem. Phys., 16*, 4147–4157. https://doi.org/10.5194/acp-16-4147-2016

Biastoch, A., Treude, T., Rüpke, L. H., Riebesell, U., Roth, C., Burwicz, E. B., Park, W., Latif, M., Böning, C. W., Madec, G., & Wallmann, K. (2011). Rising Arctic Ocean temperatures cause gas hydrate destabilization and ocean acidification. *Geophysical Research Letters, 38*(8). https://doi.org/https://doi.org/10.1029/2011GL047222

Boudreau, B. P., Luo, Y., Meysman, F. J. R., Middelburg, J. J., & Dickens, G. R. (2015). Gas hydrate dissociation prolongs acidification of the Anthropocene oceans. *Geophysical Research Letters, 42*(21), 9337-9344A. https://doi.org/https://doi.org/10.1002/2015GL065779

Boyd, D., Anka, Z., Di Primio, R., Kuhlmann, G., & De Wit, M. J. (2011). Passive margin evolution and controls on natural gas leakage in the orange basin, south Africa *South African Journal of Geology, 114*(3-4), 415-432. https://doi.org/10.2113/gssajg.114.3-4.415

Chuvilin, E., Bukhanov, B., Yurchenko, A., Davletshina, D., Shakhova, N., Spivak, E., Rusakov, V., Dudarev, O., Khaustova, N., Tikhonova, A., Gustafsson, O., Tesi, T., Martens, J., Jakobsson, M., Spasennykh, M., & Semiletov, I. (2022, 2022/04/01/). In-situ temperatures and thermal properties of the East Siberian Arctic shelf sediments: Key input for understanding the dynamics of subsea permafrost. *Marine and Petroleum Geology, 138*, 105550. https://doi.org/https://doi.org/10.1016/j.marpetgeo.2022.105550

Collett, T. S., Lee, M. W., Agena, W. F., Miller, J. J., Lewis, K. A., Zyrianova, M. V., Boswell, R., & Inks, T. L. (2011, 2//). Permafrost-associated natural gas hydrate occurrences on the Alaska North Slope. *Marine and Petroleum Geology, 28*(2), 279-294. https://doi.org/10.1016/j.marpetgeo.2009.12.001

Cramer, B., & Franke, D. (2005). INDICATIONS FOR AN ACTIVE PETROLEUM SYSTEM IN THE LAPTEV SEA, NE SIBERIA. *Journal of Petroleum Geology, 28*(4), 369-384. https://doi.org/https://doi.org/10.1111/j.1747-5457.2005.tb00088.x

Dallimore, S. R., & Collett, T. S. (2005). Summary and implications of the Mallik 2002 gas hydrate production research well program. In S. R. Dallimore & T. S. Collect (Eds.), *Scientific Results from the Mallik 2002 Gas Hydrate Production Research Well Program, Mackenzie Delta, Northwest Territories, Canada* (Vol. 585). Geological Survey of Canada.

Davie, M. K., & Buffett, B. A. (2001). A numerical model for the formation of gas hydrate below the seafloor. *Journal of Geophysical Research: Solid Earth, 106*(B1), 497-514. https://doi.org/10.1029/2000JB900363

Dlugokencky, E. J., Bruhwiler, L., White, J. W. C., Emmons, L. K., Novelli, P. C., Montzka, S. A., Masarie, K. A., Lang, P. M., Crotwell, A. M., Miller, J. B., & Gatti, L. V. (2009). Observational constraints on recent increases in the atmospheric CH4 burden. *Geophysical Research Letters, 36*(18). https://doi.org/https://doi.org/10.1029/2009GL039780

Dmitrenko, I. A., Kirillov, S. A., Tremblay, L. B., Kassens, H., Anisimov, O. A., Lavrov, S. A., Razumov, S. O., & Grigoriev, M. N. (2011). Recent changes in shelf hydrography in the Siberian Arctic: Potential for subsea permafrost instability. *Journal of Geophysical Research: Oceans, 116*(C10). https://doi.org/https://doi.org/10.1029/2011JC007218

Frederick, J. M., & Buffett, B. A. (2014). Taliks in relict submarine permafrost and methane hydrate deposits: Pathways for gas escape under present and future conditions. *Journal of Geophysical Research: Earth Surface, 119*(2), 106-122. https://doi.org/10.1002/2013JF002987

Gavrilov, A., Malakhova, V., Pizhankova, E., & Popova, A. (2020). Permafrost and Gas Hydrate Stability Zone of the Glacial Part of the East-Siberian Shelf. *Geosciences, 10*(12), 484. https://www.mdpi.com/2076-3263/10/12/484

Graw, J. H., Wood, W. T., & Phrampus, B. J. (2023). Predicting Marine In Situ Heat Flow Using a Geospatial Machine Learning Conformal Prediction. *Geochemistry, Geophysics, Geosystems, 24*(6), e2023GC010913. https://doi.org/https://doi.org/10.1029/2023GC010913

Gwiazda, R., Paull, C. K., Dallimore, S. R., Melling, H., Jin, Y. K., Hong, J. K., Riedel, M., Lundsten, E., Anderson, K., & Conway, K. (2018). Freshwater Seepage Into Sediments of the Shelf, Shelf Edge, and Continental Slope of the Canadian Beaufort Sea. *Geochemistry, Geophysics, Geosystems, 19*(9), 3039-3055. https://doi.org/https://doi.org/10.1029/2018GC007623

Hong, W.-L., Sauer, S., Panieri, G., Ambrose Jr., W. G., James, R. H., Plaza-Faverola, A., & Schneider, A. (2016). Removal of methane through hydrological, microbial, and geochemical processes in the shallow sediments of pockmarks along eastern Vestnesa Ridge (Svalbard). *Limnology and Oceanography, 61*(S1), S324-S343. https://doi.org/https://doi.org/10.1002/lno.10299

Hu, K., Issler, D. R., Chen, Z., & Brent, T. A. (2013). *Permafrost investigation by well logs, and seismic velocity and repeated shallow temperature surveys, Beaufort-Mackenzie Basin*.

Johannessen, O. M., Bengtsson, L., Miles, M. W., Kuzmina, S. I., Semenov, V. A., Alekseev, G. V., Nagurnyi, A. P., Zakharov, V. F., Bobylev, L. P., Pettersson, L. H., Hasselmann, K., & Cattle, H. P. (2004, 2004/01/01). Arctic climate change: observed and modelled temperature and sea-ice variability. *Tellus A: Dynamic Meteorology and Oceanography, 56*(4), 328-341. https://doi.org/10.3402/tellusa.v56i4.14418

Kanevskiy, M., Shur, Y., Fortier, D., Jorgenson, M. T., & Stephani, E. (2011). Cryostratigraphy of late Pleistocene syngenetic permafrost (yedoma) in northern Alaska, Itkillik River exposure. *Quaternary Research, 75*(3), 584-596. https://doi.org/10.1016/j.yqres.2010.12.003

Kätterer, T., Reichstein, M., Andrén, O., & Lomander, A. (1998, 1998/07/01). Temperature dependence of organic matter decomposition: a critical review using literature data analyzed with different models. *Biology and Fertility of Soils, 27*(3), 258-262. https://doi.org/10.1007/s003740050430

Kendall, R. A., Mitrovica, J. X., & Milne, G. A. (2005). On post-glacial sea level – II. Numerical formulation and comparative results on spherically symmetric models. *Geophysical Journal International, 161*(3), 679-706. https://doi.org/10.1111/j.1365-246X.2005.02553.x

Kleinberg, R. L., Flaum, C., Griffin, D. D., Brewer, P. G., Malby, G. E., Peltzer, E. T., & Yesinowski, J. P. (2003). Deep sea NMR: Methane hydrate growth habit in porous media and its relationship to hydraulic permeability, deposit accumulation, and submarine slope stability. *Journal of Geophysical Research: Solid Earth, 108*(B10), 2508. https://doi.org/10.1029/2003JB002389

Kleinberg, R. L., & Griffin, D. D. (2005, 6//). NMR measurements of permafrost: unfrozen water assay, pore-scale distribution of ice, and hydraulic permeability of sediments. *Cold Regions Science and Technology, 42*(1), 63-77. https://doi.org/10.1016/j.coldregions.2004.12.002

Kleinen, T., Gromov, S., Steil, B., & Brovkin, V. (2021). Atmospheric methane underestimated in future climate projections. *Environmental Research Letters, 16*, 119502. https://doi.org/10.1088/1748-9326/ac1814

Knoblauch, C., Beer, C., Liebner, S., Grigoriev, M. N., & Pfeiffer, E.-M. (2018, 2018/04/01). Methane production as key to the greenhouse gas budget of thawing permafrost. *Nature Climate Change, 8*(4), 309-312. https://doi.org/10.1038/s41558-018-0095-z

Knoblauch, C., Beer, C., Sosnin, A., Wagner, D., & Pfeiffer, E.-M. (2013). Predicting long-term carbon mineralization and trace gas production from thawing permafrost of Northeast Siberia. *Global Change Biology, 19*(4), 1160-1172. https://doi.org/https://doi.org/10.1111/gcb.12116

765
766 Kort, E. A., Wofsy, S. C., Daube, B. C., Diao, M., Elkins, J. W., Gao, R. S., Hintsa, E. J., Hurst, D. F., Jimenez,
767 R., Moore, F. L., Spackman, J. R., & Zondlo, M. A. (2012, 2012/05/01). Atmospheric observations
768 of Arctic Ocean methane emissions up to 82° north. *Nature Geoscience, 5*(5), 318-321.
769 https://doi.org/10.1038/ngeo1452

770
771 Kravchishina, M. D., Lein, A. Y., Flint, M. V., Baranov, B. V., Miroshnikov, A. Y., Dubinina, E. O., Dara, O.
772 M., Boev, A. G., & Savvichev, A. S. (2021). Methane-derived authigenic carbonates on the
773 seafloor of the Laptev Sea Shelf. *Frontiers in Marine Science, 8*.
774 https://doi.org/10.3389/fmars.2021.690304

775
776 Kvenvolden, K. A., Lilley, M. D., Lorenson, T. D., Barnes, P. W., & McLaughlin, E. (1993). The Beaufort Sea
777 continental shelf as a seasonal source of atmospheric methane. *Geophysical Research Letters,*
778 *20*(22), 2459-2462. https://doi.org/https://doi.org/10.1029/93GL02727

779
780 Liu, X., & Flemings, P. B. (2007). Dynamic multiphase flow model of hydrate formation in marine
781 sediments. *Journal of Geophysical Research: Solid Earth, 112*(B3), B03101.
782 https://doi.org/10.1029/2005JB004227

783
784 Lorenson, T. D., Greinert, J., & Coffin, R. B. (2016). Dissolved methane in the Beaufort Sea and the Arctic
785 Ocean, 1992–2009; sources and atmospheric flux. *Limnology and Oceanography, 61*(S1), S300-
786 S323. https://doi.org/https://doi.org/10.1002/lno.10457

787
788 Malakhova, V. V., & Eliseev, A. V. (2017, 2017/10/01/). The role of heat transfer time scale in the
789 evolution of the subsea permafrost and associated methane hydrates stability zone during
790 glacial cycles. *Global and Planetary Change, 157*, 18-25.
791 https://doi.org/https://doi.org/10.1016/j.gloplacha.2017.08.007

792
793 Malinverno, A. (2010). Marine gas hydrates in thin sand layers that soak up microbial methane *Earth and*
794 *Planetary Science Letters, 292*, 399-408. https://doi.org/10.1016/j.epsl.2010.02.008

795
796 McGinnis, D. F., Greinert, J., Artemov, Y., Beaubien, S. E., & Wüest, A. (2006). Fate of rising methane
797 bubbles in stratified waters: How much methane reaches the atmosphere? *Journal of*
798 *Geophysical Research: Oceans, 111*(C9). https://doi.org/https://doi.org/10.1029/2005JC003183

799
800 Miner, K. R., Turetsky, M. R., Malina, E., Bartsch, A., Tamminen, J., McGuire, A. D., Fix, A., Sweeney, C.,
801 Elder, C. D., & Miller, C. E. (2022, 2022/01/01). Permafrost carbon emissions in a changing
802 Arctic. *Nature Reviews Earth & Environment, 3*(1), 55-67. https://doi.org/10.1038/s43017-021-
803 00230-3

804

805 Moridis, G.J., Kowalsky, M.B., and Pruess, K. (2008). "TOUGH+Hydrate v1.0 user's manual: a code for the
806 simulation of system behavior in hydrate-bearing geologic media". Lawrence Berkeley National
807 Laboratory).
808
809 Muraoka, M., Ohtake, M., Susuki, N., Morita, H., Oshima, M., & Yamamoto, Y. (2019, 2019/10/01/).
810 Thermal properties of highly saturated methane hydrate-bearing sediments recovered from the
811 Krishna–Godavari Basin. *Marine and Petroleum Geology, 108*, 321-331.
812 https://doi.org/https://doi.org/10.1016/j.marpetgeo.2018.10.037
813
814 Nicolsky, D. J., Romanovsky, V. E., Romanovskii, N. N., Kholodov, A. L., Shakhova, N. E., & Semiletov, I. P.
815 (2012). Modeling sub-sea permafrost in the East Siberian Arctic Shelf: The Laptev Sea region.
816 *Journal of Geophysical Research: Earth Surface, 117*(F3).
817 https://doi.org/https://doi.org/10.1029/2012JF002358
818
819 Nicolsky, D. J., & Shakhova, N. (2010). Modeling sub-sea permafrost in the East Siberian Arctic Shelf: the
820 Dmitry Laptev Strait. *Environmental Research Letters, 5*(1), 015006.
821
822 Overduin, P. P., Liebner, S., Knoblauch, C., Günther, F., Wetterich, S., Schirrmeister, L., Hubberten, H.-W.,
823 & Grigoriev, M. N. (2015). Methane oxidation following submarine permafrost degradation:
824 Measurements from a central Laptev Sea shelf borehole. *Journal of Geophysical Research:*
825 *Biogeosciences, 120*(5), 965-978. https://doi.org/https://doi.org/10.1002/2014JG002862
826
827 Overduin, P. P., Schneider von Deimling, T., Miesner, F., Grigoriev, M. N., Ruppel, C., Vasiliev, A., Lantuit,
828 H., Juhls, B., & Westermann, S. (2019). Submarine Permafrost Map in the Arctic Modeled Using
829 1-D Transient Heat Flux (SuPerMAP). *Journal of Geophysical Research: Oceans, 124*(6), 3490-
830 3507. https://doi.org/https://doi.org/10.1029/2018JC014675
831
832 Paull, C., Dallimore, S. R., Clarke, J. H., Blasco, S., Lundsten, E., Ussler, W., Graves, D., Sherman, A.,
833 Conway, K., Melling, H., Vagle, S., & Collett, T. S. (2011). Tracking the decomposition of
834 submarine permafrost and gas hydrate under the shelf and slope of the Beaufort Sea. the 7th
835 International Conference on Gas Hydrate, Edinburgh, Scotland, U.K.
836
837 Petit, J. R., Jouzel, J., Raynaud, D., Barkov, N. I., Barnola, J. M., Basile, I., Bender, M., Chappellaz, J., Davis,
838 M., Delaygue, G., Delmotte, M., Kotlyakov, V. M., Legrand, M., Lipenkov, V. Y., Lorius, C., PÉpin,
839 L., Ritz, C., Saltzman, E., & Stievenard, M. (1999, 1999/06/01). Climate and atmospheric history
840 of the past 420,000 years from the Vostok ice core, Antarctica. *Nature, 399*(6735), 429-436.
841 https://doi.org/10.1038/20859
842
843 Pohlman, J. W., Greinert, J., Ruppel, C., Silyakova, A., Vielstädte, L., Casso, M., Mienert, J., & Bünz, S.
844 (2017). Enhanced CO2 uptake at a shallow Arctic Ocean seep field overwhelms the positive
845 warming potential of emitted methane. *Proc. Nat. Acad. Sci., 114*(21), 5355-5360.
846

Portnov, A., Smith, A. J., Mienert, J., Cherkashov, G., Rekant, P., Semenov, P., Serov, P., & Vanshtein, B. (2013). Offshore permafrost decay and massive seabed methane escape in water depths >20 m at the South Kara Sea shelf. *Geophysical Research Letters, 40*(15), 3962-3967. https://doi.org/https://doi.org/10.1002/grl.50735

Rivkina, E. M., Laurinavichus, K. S., Gilichinsky, D., & Shcherbakova, V. A. (2002). Methane generation in permafrost sediments. *Doklady Biological Sciences, 383*(6), 179-181.

Römer, M., Sahling, H., Pape, T., Bohrmann, G., & Spieß, V. (2012). Quantification of gas bubble emissions from submarine hydrocarbon seeps at the Makran continental margin (offshore Pakistan). *Journal of Geophysical Research: Oceans, 117*(C10). https://doi.org/https://doi.org/10.1029/2011JC007424

Ruppel, C. (2015, 2015/02/12). Permafrost-Associated Gas Hydrate: Is It Really Approximately 1 % of the Global System? *Journal of Chemical & Engineering Data, 60*(2), 429-436. https://doi.org/10.1021/je500770m

Ruppel, C., Hart, P. E., & Worley, C. (2010). *Degradation of subsea permafrost and associated gas hydrates offshore of Alaska in response to climate change*. http://soundwaves.usgs.gov/2010/11

Ruppel, C., & Kessler, J. D. (2017). The interaction of climate change and methane hydrates. *Reviews of Geophysics, 55*, 126-168. https://doi.org/10.1002/2016RG000534

Ruppel, C. D., Herman, B. M., Brothers, L. L., & Hart, P. E. (2016). Subsea ice-bearing permafrost on the U.S. Beaufort Margin: 2. Borehole constraints. *Geochemistry, Geophysics, Geosystems, 17*(11), 4333-4353. https://doi.org/https://doi.org/10.1002/2016GC006582

Sapart, C. J., Shakhova, N., Semiletov, I., Jansen, J., Szidat, S., Kosmach, D., Dudarev, O., van der Veen, C., Egger, M., Sergienko, V., Salyuk, A., Tumskoy, V., Tison, J. L., & Röckmann, T. (2017). The origin of methane in the East Siberian Arctic Shelf unraveled with triple isotope analysis. *Biogeosciences, 14*(9), 2283-2292. https://doi.org/10.5194/bg-14-2283-2017

Sayedi, S. S., Abbott, B. W., Thornton, B. F., Frederick, J. M., Vonk, J. E., Overduin, P., Schädel, C., Schuur, E. A. G., Bourbonnais, A., Demidov, N., Gavrilov, A., He, S., Hugelius, G., Jakobsson, M., Jones, M. C., Joung, D., Kraev, G., Macdonald, R. W., David McGuire, A., Mu, C., O'Regan, M., Schreiner, K. M., Stranne, C., Pizhankova, E., Vasiliev, A., Westermann, S., Zarnetske, J. P., Zhang, T., Ghandehari, M., Baeumler, S., Brown, B. C., & Frei, R. J. (2020, 2020/12/22). Subsea permafrost carbon stocks and climate change sensitivity estimated by expert assessment. *Environmental Research Letters, 15*(12), 124075. https://doi.org/10.1088/1748-9326/abcc29

887 Schuur, E. A. G., Bockheim, J., Canadell, J. G., Euskirchen, E., Field, C. B., Goryachkin, S. V., Hagemann, S.,
888 Kuhry, P., Lafleur, P. M., Lee, H., Mazhitova, G., Nelson, F. E., Rinke, A., Romanovsky, V. E.,
889 Shiklomanov, N., Tarnocai, C., Venevsky, S., Vogel, J. G., & Zimov, S. A. (2008). Vulnerability of
890 Permafrost Carbon to Climate Change: Implications for the Global Carbon Cycle. *BioScience,*
891 *58*(8), 701-714. https://doi.org/10.1641/b580807

892
893 Schuur, E. A. G., McGuire, A. D., Schädel, C., Grosse, G., Harden, J. W., Hayes, D. J., Hugelius, G., Koven,
894 C. D., Kuhry, P., Lawrence, D. M., Natali, S. M., Olefeldt, D., Romanovsky, V. E., Schaefer, K.,
895 Turetsky, M. R., Treat, C. C., & Vonk, J. E. (2015, 2015/04/01). Climate change and the
896 permafrost carbon feedback. *Nature, 520*(7546), 171-179. https://doi.org/10.1038/nature14338

897
898 Sergienko, V. I., Lobkovskii, L. I., Semiletov, I. P., Dudarev, O. V., Dmitrievskii, N. N., Shakhova, N. E.,
899 Romanovskii, N. N., Kosmach, D. A., Nikol'skii, D. N., Nikiforov, S. L., Salomatin, A. S., Anan'ev, R.
900 A., Roslyakov, A. G., Salyuk, A. N., Karnaukh, V. V., Chernykh, D. B., Tumskoi, V. E., Yusupov, V. I.,
901 Kurilenko, A. V., Chuvilin, E. M., & Bukhanov, B. A. (2012, 2012/09/01). The degradation of
902 submarine permafrost and the destruction of hydrates on the shelf of east arctic seas as a
903 potential cause of the "Methane Catastrophe": some results of integrated studies in 2011.
904 *Doklady Earth Sciences, 446*(1), 1132-1137. https://doi.org/10.1134/S1028334X12080144

905
906 Serov, P., Portnov, A., Mienert, J., Semenov, P., & Ilatovskaya, P. (2015). Methane release from pingo-
907 like features across the South Kara Sea shelf, an area of thawing offshore permafrost. *Journal of*
908 *Geophysical Research: Earth Surface, 120*(8), 1515-1529.
909 https://doi.org/https://doi.org/10.1002/2015JF003467

910
911 Serreze, M. C., & Francis, J. A. (2006, 2006/06/01). The Arctic Amplification Debate. *Climatic Change,*
912 *76*(3), 241-264. https://doi.org/10.1007/s10584-005-9017-y

913
914 Shakhova, N., Semiletov, I., & Chuvilin, E. (2019). Understanding the Permafrost–Hydrate System and
915 Associated Methane Releases in the East Siberian Arctic Shelf. *Geosciences, 9*(6), 251.
916 https://www.mdpi.com/2076-3263/9/6/251

917
918 Shakhova, N., Semiletov, I., Leifer, I., Salyuk, A., Rekant, P., & Kosmach, D. (2010). Geochemical and
919 geophysical evidence of methane release over the East Siberian Arctic Shelf. *J. Geophys. Res.,*
920 *115*(C08007).

921
922 Shakhova, N., Semiletov, I., Salyuk, A., Yusupov, V., Kosmach, D., & Gustafsson, O. (2010). Extensive
923 methane venting to the atmosphere from sediments of the East Siberian Arctic Shelf. *Science,*
924 *327*, 1246-1250.

925
926 Shakhova, N., Semiletov, I., Sergienko, V., Lobkovsky, L., Yusupov, V., Salyuk, A., Salomatin, A., Chernykh,
927 D., Kosmach, D., Panteleev, G., Nicolsky, D., Samarkin, V., Joye, S., Charkin, A., Dudarev, O.,
928 Meluzov, A., & Gustafsson, O. (2015). The East Siberian Arctic Shelf: towards further assessment

of permafrost-related methane fluxes and role of sea ice. *Philosophical Transactions of the Royal Society A: Mathematical, Physical and Engineering Sciences, 373*(2052), 20140451. https://doi.org/doi:10.1098/rsta.2014.0451

Skarke, A., Ruppel, C., Kodis, M., Brothers, D., & Lobecker, E. (2014, 08/24/online). Widespread methane leakage from the sea floor on the northern US Atlantic margin. *Nature Geoscience, 7*, 657. https://doi.org/10.1038/ngeo2232

Sloan, E. D., & Koh, C. (2007). *Clathrate Hydrates of Natural Gases*. CRC Press.

Smith, A. J., Flemings, P. B., & Fulton, P. M. (2014, 2014/06/01/). Hydrocarbon flux from natural deepwater Gulf of Mexico vents. *Earth and Planetary Science Letters, 395*, 241-253. https://doi.org/10.1016/j.epsl.2014.03.055

Smith, L., Savage, A., Flemings, P. B., Colwell, F., Mikucki, J., & You, K. (2022). *Too much pressure: Effect of sediment compaction on microbial viability* Astrobiology Science Conference, Atlanta, GA, USA.

Sowers, T. (2006). Late Quaternary atmospheric CH4 isotope record suggests marine clathrates are stable, . *Science, 311*(5762), 838-840. https://doi.org/10.1126/science.1121235

Sparrow, K. J., Kessler, J. D., Southon, J. R., Garcia-Tigreros, F., Schreiner, K. M., Ruppel, C. D., Miller, J. B., Lehman, S. J., & Xu, X. (2018). Limited contribution of ancient methane to surface waters of the U.S. Beaufort Sea shelf. *Science Advances, 4*(1), eaao4842. https://doi.org/doi:10.1126/sciadv.aao4842

Steinbach, J., Holmstrand, H., Shcherbakova, K., Kosmach, D., Brüchert, V., Shakhova, N., Salyuk, A., Sapart, C. J., Chernykh, D., Noormets, R., Semiletov, I., & Gustafsson, Ö. (2021). Source apportionment of methane escaping the subsea permafrost system in the outer Eurasian Arctic Shelf. *Proceedings of the National Academy of Sciences, 118*(10), e2019672118. https://doi.org/10.1073/pnas.2019672118

Stranne, C., O'Regan, M., Jakobsson, M., Brüchert, V., & Ketzer, M. (2019). Can anaerobic oxidation of methane prevent seafloor gas escape in a warming climate? *Solid Earth, 10*(5), 1541-1554. https://doi.org/10.5194/se-10-1541-2019

Strauss, J., Laboor, S., Schirrmeister, L., Fedorov, A. N., Fortier, D., Froese, D., Fuchs, M., Günther, F., Grigoriev, M. N., Harden, J. W., Hugelius, G., Jongejans, L. L., Kanevskiy, M., Kholodov, A. L., Kunitsky, V., Kraev, G., Lozhkin, A., Rivkina, E., Shur, Y., Siegert, C., Spektor, V., Streletskaya, I., Ulrich, M., Vartanyan, S., Veremeeva, A., Walter Anthony, K. M., Wetterich, S., Zimov, N., &

Grosse, G. (2021). Circum-Arctic map of the Yedoma permafrost domain. *Frontiers in Earth Science, 9*(758360). https://doi.org/ 10.3389/feart.2021.758360

Sun, X., & Mohanty, K. K. (2006). Kinetic simulation of methane hydrate formaiton and dissociation in porous media. *Chemical Engineering Science, 61*, 3476-3495. https://doi.org/10.1016/j.ces.2005.12.017

Thornton, B. F., Geibel, M. C., Crill, P. M., Humborg, C., & Mörth, C.-M. (2016). Methane fluxes from the sea to the atmosphere across the Siberian shelf seas. *Geophysical Research Letters, 43*(11), 5869-5877. https://doi.org/https://doi.org/10.1002/2016GL068977

Vonk, J. E., Mann, P. J., Davydov, S., Davydova, A., Spencer, R. G. M., Schade, J., Sobczak, W. V., Zimov, N., Zimov, S., Bulygina, E., Eglinton, T. I., & Holmes, R. M. (2013). High biolability of ancient permafrost carbon upon thaw. *Geophysical Research Letters, 40*(11), 2689-2693. https://doi.org/https://doi.org/10.1002/grl.50348

Waite, W. F., Santamarina, J. C., Cortes, D. D., Dugan, B., Espinoza, D. N., Germaine, J., Jang, J., Jung, J. W., Kneafsey, T. J., Shin, H., Soga, K., Winters, W. J., & Yun, T. S. (2009). Physical properties of hydrate-bearing sediments. *Reviews of Geophysics, 47*, RG4003. https://doi.org/8755-1209/09/2008RG000279

Walter Anthony, K., Daanen, R., Anthony, P., Schneider von Deimling, T., Ping, C.-L., Chanton, J. P., & Grosse, G. (2016, 2016/09/01). Methane emissions proportional to permafrost carbon thawed in Arctic lakes since the 1950s. *Nature Geoscience, 9*(9), 679-682. https://doi.org/10.1038/ngeo2795

Walter Anthony, K. M., Anthony, P., Grosse, G., & Chanton, J. (2012, 2012/06/01). Geologic methane seeps along boundaries of Arctic permafrost thaw and melting glaciers. *Nature Geoscience, 5*(6), 419-426. https://doi.org/10.1038/ngeo1480

Walter Anthony, K. M., Lindgren, P., Hanke, P., Engram, M., Anthony, P., Daanen, R., Bondurant, A., Liljedahl, A. K., Lenz, J., Grosse, G., Jones, B. M., Brosius, L., James, S. R., Minsley, B. J., Pastick, N. J., Munk, J., Chanton, J. P., Miller, C. E., & Meyer, F. J. (2021). Decadal-scale hotspot methane ebullition within lakes following abrupt permafrost thaw. *Environmental Research Letters, 16*, 035010. https://doi.org/10.1088/1748-9326/abc848

Wang, B., Jun, I., Socolofsky, S. A., DiMarco, S. F., & Kessler, J. D. (2020). Dynamics of Gas Bubbles From a Submarine Hydrocarbon Seep Within the Hydrate Stability Zone. *Geophysical Research Letters, 47*(18), e2020GL089256. https://doi.org/https://doi.org/10.1029/2020GL089256

Wang, B., Socolofsky, S. A., Breier, J. A., & Seewald, J. S. (2016). Observations of bubbles in natural seep flares at MC 118 and GC 600 using in situ quantitative imaging. *Journal of Geophysical Research: Oceans, 121*(4), 2203-2230. https://doi.org/https://doi.org/10.1002/2015JC011452

Wilkenskjeld, S., Miesner, F., Overduin, P. P., Puglini, M., & Brovkin, V. (2022). Strong increase in thawing of subsea permafrost in the 22nd century caused by anthropogenic climate change. *The Cryosphere, 16*(3), 1057-1069. https://doi.org/10.5194/tc-16-1057-2022

Wright, J. F., Nixon, F. M., Dallimore, S. R., & Cote, M. M. (2005). Thermal conductivity of seidments within the gas-hydrate-bearing interval at the JAPEX/JNOC/GSC et al. Mallik 5K-38 gas hydrate production research well. In S. R. Dallimore & T. S. Collect (Eds.), *Scientific Results from the Mallik 2002 Gas Hydrate Production Research Program, Mackenzie Delta, Northwest Territories, Canada* (Vol. Bulletin 585). Geological Survey of Canada.

You, K., & Flemings, P. B. (2018). Methane hydrate formation in thick sandstones by free gas flow. *Journal of Geophysical Research: Solid Earth, 123*. https://doi.org/org/10.1029/2018JB015683

You, K., & Flemings, P. B. (2021). Methane Hydrate Formation and Evolution During Sedimentation. *Journal of Geophysical Research: Solid Earth, 126*(4), e2020JB021235. https://doi.org/https://doi.org/10.1029/2020JB021235

You, K., Flemings, P. B., Malinverno, A., Collett, T., & Darnell, K. N. (2019). Mechanisms of methane hydrate formation in geological system. *Reviews of Geophysics, 57*. https://doi.org/10.1029/2018RG000638

You, K., Summa, L., Flemings, P., Santra, M., & Fang, Y. (2021). Three-Dimensional Free Gas Flow Focuses Basin-Wide Microbial Methane to Concentrated Methane Hydrate Reservoirs in Geological System. *Journal of Geophysical Research: Solid Earth, 126*(12), e2021JB022793. https://doi.org/https://doi.org/10.1029/2021JB022793

Zimov, S., Schuur, E. A. G., & Chapin III, F. S. (2006). Permafrost and the global carbon budget. *Science, 312*(5780).

Zimov, S. A., Voropaev, Y. V., Semiletov, I. P., Davidov, S. P., Prosiannikov, S. F., Chapin, F. S., Chapin, M. C., Trumbore, S., & Tyler, S. (1997). North Siberian Lakes: A Methane Source Fueled by Pleistocene Carbon. *Science, 277*(5327), 800-802. https://doi.org/doi:10.1126/science.277.5327.800

1048

1049

1050

1051

1052